

Sassy Title

by

E. Ross



A thesis submitted to the
University of Birmingham
for the degree of
DOCTOR OF PHILOSOPHY

Solar and Stellar Physics Group (SASP)
School of Physics and Astronomy
University of Birmingham
Birmingham, B15 2TT
Month 20XX

Abstract

You're awesome. Make sure the examiners know it

Acknowledgements

Who do you hate least?

Contents

1 Investigations into the Morphology of the Solar Mean Magnetic Field	1
1.1 Introduction	1
1.2 Aims	5
1.3 Data	5
1.4 Methodology	12
1.5 Results	16
1.6 Discussion	24
1.7 Conclusion	32
2 Rossby Modes in the Solar Mean Magnetic Field	35
2.1 Introduction	35
2.2 Aims	37
2.3 Theory	38
2.4 Methodology	39
2.5 Results	42
2.6 Discussion	45
2.7 Conclusion	51
A Simulations of the Artificial SMMF	54
A.1 Model	54
A.2 Configuration of the Simulations	56
A.3 Outputs	59
Bibliography	60

List of Figures

1.1	An example of the BiSON ratios data over a 30-minute period. The separation between the two ratios is due to the solar mean magnetic field.	8
1.2	(a) 40-second cadence observations of the SMMF from the Sutherland BiSON station between 1992 and 2012. The sense of the field was chosen to match the Chaplin et al. (2003) and the WSO observations, where positive is for a field pointing outwards from the Sun. (b) Power spectrum of the SMMF on a 40-second cadence truncated to $10\mu\text{Hz}$, however the nyquist frequency is 12.5 mHz .	10
1.3	Daily averaged SMMF measured by WSO (blue) and by the Sutherland BiSON station (black).	11
1.4	Comparisons between the BiSON SMMF data and the WSO SMMF data. (a) shows the correlation between daily averaged BiSON SMMF and the WSO SMMF. The green line provides the fit to the data, while the red line shows a 1:1 relation for comparison. (b) shows a comparison between the power spectra of BiSON and SMMF.	12
1.5	Full power spectrum of the BiSON SMMF on a logarithmic scale up to the Nyquist frequency.	13
1.6	Locations of aliased power in side-band peaks. The orange dotted-lines show the locations of frequencies at multiples of 1/day. The green dashed-lines show the location of the side-band peaks – harmonic frequencies reflected around multiples of 1/day. The inset shows a zoom of one set of side-band peaks around 1/day.	17
1.7	Shows the effects of the window function on the power spectrum. Black line: BiSON SMMF PSD; dark orange line: power spectrum of the window function; blue and light orange lines: the power spectrum of the artificial data without and with gaps, respectively; pink line: the input peak used to generate the artificial data.	19
1.8	...	24
1.9	...	26
1.10	...	27

1.11	(a) Shows the peak distribution before and after the time-averaged broadening, and the fit to the broadened peak. (b) Shows the peak distribution before and after the analytical broadening, and the fit to the broadened peak. In both plots the broadened peaks have been shifted by the relevant frequency to overlay them on top of the true ν_0 for comparison.	31
1.12	33
1.13	34
2.1	Model fit to the full BiSON SMMF PSD.	37
2.2	Residual power spectrum of the BiSON SMMF. Over plotted in the green curve is the model of the main SMMF signal. Also over plotted as vertical solid lines are the expected locations of the 4 lowest-frequency sectoral r modes and the dashed lines, the locations of the B_0 variation frequency splitting.	42
2.3	Realisations of the statistics tests of BiSON data for different re-binning factors (n). The panels of each sub figure are: (top) the full PSD and fit, (second panel) the full and re-binned residuals, (third panel) the probability of statistical noise in each bin, (bottom) distribution of the residuals compared to a χ^2 2n-DOF.	44
2.4	Model fit to the r mode in the BiSON PSD residuals using the median from the parameter posterior distributions.	46
2.5	Mode displacement schematic for an $l = m = 2$ r mode (Strohmayer & Mahmoodifar, 2014)	47
2.6	Time series of the velocity and amplitude modulation toy model simulations. The blue curve shows the velocity modulation, i.e. modulating using a cosine with period of 1 year, whereas the orange curve shows the amplitude modulation, i.e. modulating using a rectified cosine with period 1 year.	48
2.7	Power spectra for the two modulation methods, showing the difference in the way the modulation has changed the frequency of the observed mode.	48
2.8	SDO/HMI SMMF split into hemispheres and compared to other SMMF sources during (a) 2011, and (b) 2014. The top panel in each figure shows the north (N), south (S), and total disk-averaged mean magnetic field, for both the full solar disk and from pixels within 99% of solar radius. The bottom panels show a comparison between the SMMF, as observed BiSON, Wilcox Solar Observatory (WSO), and HMI (full disk and the 99% disk).	49
2.9	Comparison of the power spectra for BiSON, WSO, and SDO/HMI. In both figures, the top panel shows the BiSON PSD and the bottom panel shows either the WSO or HMI PSD. The dashed, black line shows the location of theoretical $l = 2 = m$ r mode frequency, and the red, solid line shows the location of the peak fit in the BiSON PSD residuals.	51

A.1	Schematic representations of the two models of the artificial SMMF. (a) shows the cosine model with a single source of constant polarity transiting the visible disc. (b) shown the sign change model whereby there are 2 regions of opposite polarity transiting the disc, and their contribution to the SMMF changes during the transit.	55
A.2	A single realisation of (a) the cosine model, and (b) the sign change model.	56
A.3		57
A.4	(a) the burn-in period required to ensure that the interference of sources stabilises. (b) histogram of the number of sources which re- main in the simulation (out of the 20000 input), after the burn-in is removed. (c)	58
A.5	Limit spectrum from 100 realisations of the cosine model (a) and the sign change model (b) using a single source in each model.	59

List of Tables

1.1	Median values of the marginalised posterior distributions for each model parameter in the fit to the BiSON power spectrum. Numbers in brackets denote uncertainties on the last 2 digits, and all uncertainties correspond to the 68% credible intervals either side of the median. . .	22
1.2	Median values of the marginalised posterior distributions for each model parameter in the fit to the WSO power spectrum. Numbers in brackets denote uncertainties on the last 2 digits, and all uncertainties correspond to the 68% credible intervals either side of the median. . .	23
2.1	Predicted ⁺ and observed [◦] r mode frequencies for combinations of l and m . Predicted frequencies and conversions of observations to different frames of reference use equation (2.1), equation (2.2), and equation (2.3), with $\Omega = 453.1$ nHz. The predicted splitting for the B_0 angle variation is also provided. The key for the source column is: LPT for Löptien et al. (2018), LNG for Liang et al. (2019), and LZA for Lanza et al. (2019).	39
2.2	Median posterior values of the Lorentzian model for the r-mode peak in the BiSON SMMF PSD residuals. Numbers in brackets denote uncertainties on the last 2 digits, and all uncertainties correspond to the 68% credible intervals either side of the median.	43

Abbreviations

ADC	Analogue to Digital Converter
AS	Air Shower
AVD	Asymptotic Viewing Direction
BiSON	Birmingham Solar Oscillations Network
CMA	Central Moving Average
CME	Coronal Mass Ejection
CR	Cosmic Ray
EAS	Extensive Air Shower
EV	Enhanced Variance
FD	Forbush Decrease
FE	Forbush Effect
FOV	Field Of View
GCR	Galactic Cosmic Ray
GIC	Ground Induced Current
GLE	Ground Level Enhancement
GMDN	Global Muon Detector Network
GNSS	Global Navigation Satellite System
GZK	Greisen-Zatsepin-Kuzmin
HCS	Heliospheric Current Sheet
HiSPARC	High School Project on Astrophysics and Research with Cosmics
ICME	Interplanetary Coronal Mass Ejection
IMF	Interplanetary Magnetic Field
LC	Loss Cone
MD	Muon Detector
MFP	Mean Free Path
MIP	Minimum Ionising Particle
MOSWOC	Met Office Space Weather Operations Centre
MPV	Most Probable Value
NM	Neutron Monitor
NMDB	Neutron Monitor Data Base
NOAA	National Oceanic and Atmospheric Administration
PCA	Principal Component Analysis
PCR	Primary Cosmic Ray
PMT	Photo Multiplier Tube
RSS	Resonant Scattering Spectrometer
SCR	Solar Cosmics Ray
SEP	Solar Energetic Particle
SMMF	Solar Mean Magnetic Field
SSC	Storm Sudden Commencement
SSN	Sun-Spot Number
SWPC	Space Weather Prediction Center
WSO	Wilcox Solar Observatory

1 Investigations into the Morphology of the Solar Mean Magnetic Field

1.1 Introduction

The Sun has a complicated magnetic field structure; many features of the Sun and proxies for the solar activity are related to the evolution of the Sun's magnetic field (Wu et al., 2018).

The solar mean magnetic field (SMMF) is a surprising, non-zero measurement of the imbalance of opposite magnetic flux polarities observed on the full, visible disk of the Sun (Svalgaard et al., 1975), and is defined as the mean line-of-sight (LOS) magnetic field when observing the Sun-as-a-star (Scherrer et al., 1977a,b; Garca et al., 1999). In the literature the SMMF is also commonly referred to as the general magnetic field (GMF) (Severny, 1971) or the mean magnetic field (MMF) (Kotov, 2008) of the Sun.

Observations of the SMMF have typically been made by measuring the Zeeman splitting of spectral lines using a Babcock-type magnetograph (Scherrer et al., 1977a), although more recently the SMMF has been calculated from full-disk LOS magnetograms taken from space-borne telescopes such as the Solar Dynamic Observatory Helioseismic and Magnetic Imager (SDO/HMI), in order to understand the morphology of the SMMF (Kutsenko et al., 2017; Bose & Nagaraju, 2018). It is understood that the strength of the SMMF may vary depending on the spectral line

used to measure the SMMF (Kotov, 2008, 2012), however it is generally accepted in the literature that the SMMF varies slowly with the solar activity cycle, with a amplitude of up to around ± 2 G during solar maximum and ± 0.2 G during solar minimum (Plachinda et al., 2011). In addition, the SMMF displays a strong, quasi-coherent rotational signal (Chaplin et al., 2003; Xie et al., 2017), which we assume arises from inhomogeneities on the solar disk with lifetimes of a few rotations.

Despite a wide-ranging existing literature on SMMF observations, spanning several decades, ultimately, our understanding is limited and the SMMF origin remains a crucial, open question in solar physics. The principle component of the SMMF is commonly assumed to be weak, large-scale magnetic flux, distributed over the entire solar disk, rather than active regions (ARs) or sunspots (Severny, 1971; Scherrer et al., 1977a; Xiang & Qu, 2016). However conversely, Scherrer et al. (1972) found that the SMMF was most highly correlated with only the inner-most one quarter, by area, of the solar disk, which is more sensitive to active latitudes.

In recent literature, Bose & Nagaraju (2018) provided an interesting and novel approach to understanding the SMMF whereby they dissected the SMMF by feature identification and pixel-by-pixel analysis of full-disk magnetograms. Bose & Nagaraju (2018) concluded that: (i) the observed variability in the SMMF lies in the polarity imbalance of large-scale magnetic field structures on the visible surface of the Sun, (ii) the correlation between the flux from sunspots and the SMMF is statistically insignificant, (iii) and more critically that the background flux dominates the SMMF, accounting for around 89% of the variation in the SMMF. There still remained a strong component due to rotation in the background magnetic field presented by Bose & Nagaraju (2018), which is indicative of inhomogeneous magnetic features with lifetimes on the order of several solar rotations rather than the shorter-lived, weaker fields usually associated with the large-scale background.

In order to identify the contours of specific features Bose & Nagaraju (2018) used an adaptive thresholding technique on various SDO/AIA images of the solar

disc to create binary masks for different types of features. These masks were then applied to scaled SDO/HMI magnetograms in order to segment which features contributed to the SMMF. Upon a closer inspection of the example magnetogram in Figure 2 of the paper, with overplotted contours of identified features, there are clearly regions of strong magnetic flux concentrations in the local vicinity of, and connected to, the identified features that are outside of the contour lines and therefore are allocated to the background magnetic field. It seems an obvious statement to suggest that optical counterparts of the magnetograms will not exactly align with the observed flux in the magnetograms; it should be expected that the magnetic field will manifest itself differently in the optical observations and the magnetograms, which leads one to believe that the background component in this study could mistakenly contain flux from some of the identified features.

In particular, there was a careful treatment of plages in this work from additional chromospheric observations, however a separate handling of faculae in the photosphere was absent from the study, which are well-known to exhibit long lifetimes [CITE]. Including faculae could have contributed to the completeness of the study. Furthermore, a segmentation of the identified background component into regions of strong and weak field would provide more clarity on the exact morphology of the SMMF, and would have likely provided evidence to conclude whether flux from AR features were incorporated into the background.

Despite these findings, it is known that the strength of the SMMF is weaker during solar minimum, when there are fewer ARs, and stronger during solar maximum, when there are more ARs. This is suggestive that the processes which underpin the evolution of ARs affect the SMMF.

There is another view in the literature which suggests AR flux dominates the SMMF. It was shown earlier by Kutsenko et al. (2017) that a large component of the SMMF may be explained by strong and intermediate flux regions, that are associated with ARs. Again using a thresholding technique, they showed between 65%

to 95% of the SMMF could be attributed to strong and intermediate flux, while the fraction of the occupied area varied between 2% to 6% of the disk area, depending on the chosen threshold for separating weak and strong flux. This finding suggests that strong, long-lived inhomogeneous regions of magnetic field produce the strong rotation signal in the SMMF. Potential sources could be sunspots, plages, faculae, etc. and Kutsenko et al. (2017) discuss however that there is an entanglement of strong flux (typically associated with ARs) and intermediate flux (typically associated with network fields and remains of decayed ARs). Disentangling the flux would have provided a more accurate analysis of the SMMF owing to a clearer picture of the main contributor to the SMMF.

The Sun’s dynamo and hence magnetic field is directly coupled to the solar rotation. The Sun exhibits latitude-dependent and depth-dependent differential rotation with a sidereal, equatorial period of around 25 days (Howe, 2009). To Earth-based observers, the synodic rotation of the Sun is observed at around 27 days, and the SMMF displays a dominant periodicity of around 27 days due to the solar rotation (Chaplin et al., 2003; Xie et al., 2017; Bose & Nagaraju, 2018). It was also reported by Xie et al. (2017) that the differential solar rotation was observed in the SMMF with measured rotational periods of 28.28 ± 0.67 days and 27.32 ± 0.64 days for the rising and declining phases, respectively, of all of the solar cycles in their considered time-frame.

On the other hand, Xiang & Qu (2016) utilise ensemble empirical mode decomposition (EEMD) analysis to extract modes of the SMMF and find two rotation periods which are derived from different strengths of magnetic flux elements. They found that a rotation period of 26.6 days was related to a weaker magnetic flux element within the SMMF, while for stronger magnetic flux elements in the SMMF, the measured rotation period is 28.5 days.

Ultimately, to date, our understanding of the SMMF and its origin remains rather limited.

1.2 Aims

In this work an investigation of high-cadence (sub-minute) observations of the SMMF, made by the Birmingham Solar Oscillations Network (BiSON) (Chaplin et al., 1996, 2005; Hale et al., 2016), was performed. The aim of the investigation was to understand the morphology of the SMMF.

This work provides a frequency domain analysis of the SMMF data, where a model was built up and fit to the power spectrum of the SMMF which allowed us to understand the characteristics of its possible source(s).

The rotational modulation signal in the SMMF was clearly observed as several low-frequency peaks in the power spectrum. In addition, the use of the high-cadence data was especially crucial for inferences on components of the SMMF with periods of less than a day at higher frequencies in the power spectrum, with the intention to determine whether the background magnetic field exhibited a stochastically excited component, which evolved on short timescales.

After fitting a model of the power spectrum, artificial data was simulated and comparisons were made to other sources of SMMF data to aid the clarification of the inferences against the observations.

1.3 Data

1.3.1 Summary of the Data Set

Chaplin et al. (2003) provided the first examination of the SMMF using data from the Birmingham Solar Oscillations Network (BiSON), and the work presented in this paper is a continuation of that study.

BiSON is a six-station, ground-based, global network of telescopes attempting to continuously monitor the Sun, which principally makes precise measurements of the line-of-sight (LOS) velocity of the photosphere due to solar p mode oscillations. Through the use of polarising optics and additional electronics, the BiSON spec-

trometers can measure both the disc-averaged LOS velocity and magnetic field in the photosphere (Chaplin et al., 2003), however not all BiSON sites measure the SMMF.

In this study we focus on the data collected by the Sutherland node, in South Africa, which was also used by Chaplin et al. (2003). Data are sampled on a 40-second cadence, and the SMMF data collected by the Sutherland station pertains the epochs from 01/1992 – 12/2012. Over this period, the duty cycle of solar observation is low because of the single-site observations, and averages to be $\sim 15.6\%$ of the total epoch.

As a comparison to the BiSON data, SMMF observations were also acquired from the Wilcox Solar Observatory (WSO) (<http://wso.stanford.edu/>) (Scherrer et al., 1977b). The WSO SMMF data are sampled daily from 16/05/1975 – present day, but for comparison with the BiSON SMMF, we used data over the same temporal range.

The WSO also measures the LOS SMMF Sun using a Babcock-type magnetograph, which allows the measurement of amount and sense of circular polarisation in the wings in an absorption line (Scherrer et al., 1977a). WSO uses two absorption lines for measurement of the field: the Fe I at 5250 Å($\lambda 5250$) is used for measurement of the field, and FE I at 5124 Å($\lambda 5124$) is used to determine the instrument’s zero offset, as this line is magnetically insensitive. Scherrer et al. (1977a) describes that a single, complete observation takes ~ 20 minutes, consisting of four 3-minute integrations. The data provided by WSO is a daily weighted mean of the observations, where the weighting used is the statistical uncertainty and the magnitude of the zero offset measured with the $\lambda 5124$ line.

1.3.2 Obtaining the SMMF from BiSON

To acquire the SMMF from BiSON data, the method as described by Chaplin et al. (2003) was adopted; here we discuss the key aspects.

Each BiSON site employs a resonant scattering spectrometer (RSS) to measure the Doppler shift of the $^2\text{S}_{1/2} \rightarrow ^2\text{P}_{1/2}$ line (D1 line) of potassium, at ~ 770 nm (Brookes et al., 1978). A potassium vapour cell placed within a longitudinal magnetic field Zeeman splits the laboratory line into the two allowed D1 transitions (Lund et al., 2017). The intensity of the longer wavelength (red; I_R) and shorter wavelength (blue; I_B) components of the line may be measured by the RSS almost simultaneously, by using polarising optics to switch between the red and blue wings of the line, to form the ratio given by equation (1.1) which is used as a proxy for the Doppler shift from the LOS velocity of the photosphere (see Brookes et al. (1976, 1978); Elsworth et al. (1995a); Chaplin et al. (2003); Lund et al. (2017)).

$$\mathcal{R} = \frac{I_B - I_R}{I_B + I_R} \quad (1.1)$$

There are known effects which occur when making observations of the entire solar disk at one time, such as LOS Doppler-imaging and limb-darkening (Davies et al., 2014b). Some BiSON stations, that do not measure the SMMF, use optics to spatially scramble incoming sunlight to remove Doppler-imaging effects, to ensure a more accurate measure of the disk-averaged Sun-as-a-star. Sutherland however, is not free from these effects, but they are assumed to be small in the analysis.

Photospheric magnetic fields Zeeman split the Fraunhofer line and the Zeeman-split components have opposite senses of circular polarization (Chaplin et al., 2003). Additional polarising optics are used in the RSS to manipulate the sense of circular polarization (either + or -) that is passed through the instrument. The ratio \mathcal{R}_+ or \mathcal{R}_- is formed, and the ratios \mathcal{R}_\pm would be equal if there was no magnetic field present.

The observed ratio (\mathcal{R}_\pm) may be decomposed as given by equation (1.2); where \mathcal{R}_{orb} is the radial component of the Earth's orbital velocity around the Sun, $\mathcal{R}_{\text{spin}}$ is the component towards the Sun of the Earth's diurnal rotation about its spin axis as a function of latitude and time, \mathcal{R}_{grs} is from the gravitational red-shift of the

solar line due to the Sun's mass (Elsworth et al., 1995b; Dumbill, 1999). The LOS velocity due to p mode oscillations are given by $\delta r_{\text{osc}}(t)$, and $\delta r_B(t)$ is due to the magnetic field (+/- from the polarity) (Dumbill, 1999). The effect of the magnetic field on the ratio is shown in Fig. 1.1, and it is clear to see from equation (1.3) that the difference between the opposite magnetic field ratios is twice the magnetic ratio residual.

$$\mathcal{R}_{\pm} = \mathcal{R}_{\text{orb}} + \mathcal{R}_{\text{spin}} + \mathcal{R}_{\text{grs}} + \delta r_{\text{osc}}(t) \pm \delta r_B(t) \quad (1.2)$$

$$\mathcal{R}_+ - \mathcal{R}_- = 2 \delta r_B(t) \quad (1.3)$$

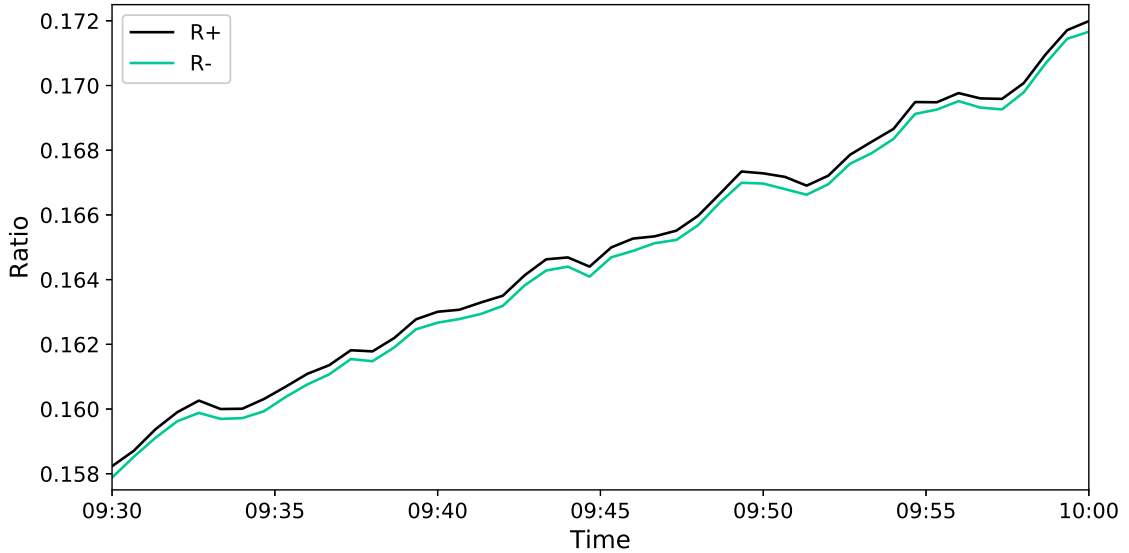


Figure 1.1: An example of the BiSON ratios data over a 30-minute period. The separation between the two ratios is due to the solar mean magnetic field.

In fact, the BiSON RSS is measuring the velocity variation on the solar disk, and therefore a calibration from the ratio to a velocity is necessary. One method of calibration is achieved by first fitting the observed ratio, averaged over both magnetic polarities, to a 2nd- or 3rd-order polynomial as a function of velocity, as discussed by Elsworth et al. (1995b). Here we chose to fit the ratio in terms of velocity, $\mathcal{R}_{\text{calc}}(u)$, see equation (1.4):

$$\mathcal{R}_{\text{calc}}(u) = \sum_n \mathcal{R}_n u^n \quad (1.4)$$

where:

$$u = v_{\text{orb}} + v_{\text{spin}} \quad (1.5)$$

and v_{orb} is the velocity component related to the ratio, \mathcal{R}_{orb} ; v_{spin} is related to the ratio, $\mathcal{R}_{\text{spin}}$; and n is the polynomial order.

It is possible to see that through the removal of $\mathcal{R}_{\text{calc}}(u)$ from the observed ratios, one is left with the ratio residuals of the p mode oscillations and the magnetic field (see equation (1.6)). Conversion from ratio residuals into velocity residuals uses the calibration given by equation (1.7).

$$\mathcal{R}_{\pm} - \mathcal{R}_{\text{calc}}(u) = \delta r_{\text{osc}}(t) \pm \delta r_{\text{B}}(t) \quad (1.6)$$

$$\delta v(t) = \left(\frac{d\mathcal{R}_{\text{calc}}}{dV} \right)^{-1} \delta r(t) \quad (1.7)$$

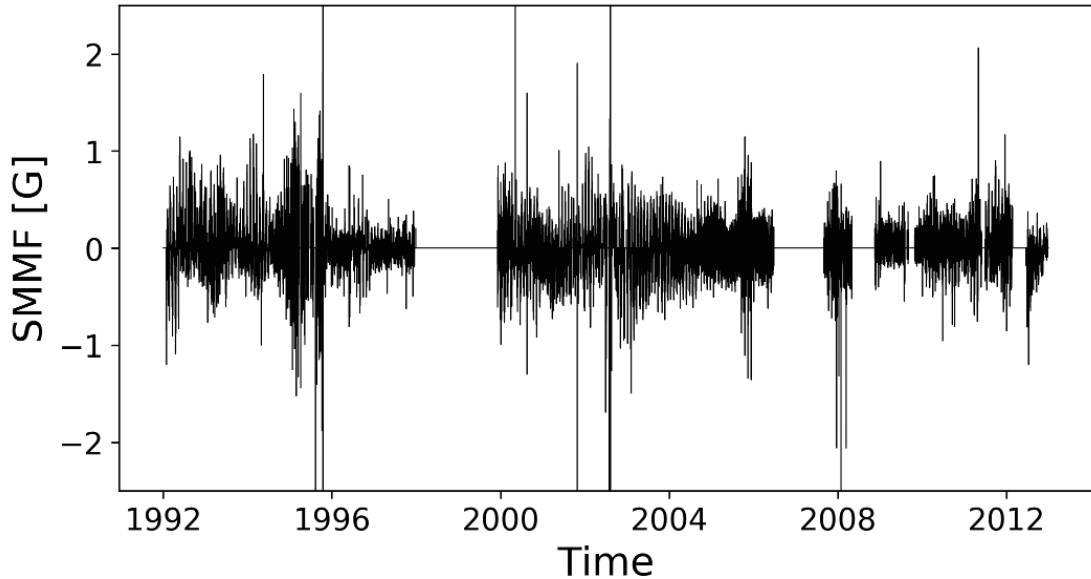
In order to finally obtain the SMMF in units of magnetic field, one must combine equation (1.3) and equation (1.7) with the conversion factor in equation (1.8) (Dumbill, 1999), where μ_B is the Bohr magneton, h is Planck's constant, c is the speed of light, and ν is the frequency of the photons, and the entire procedure can be simplified into equation (1.9).

$$K_B = \frac{8}{3} \frac{\mu_B}{h} \frac{c}{\nu} \approx 2.89... \text{ ms}^{-1} \text{ G}^{-1} \quad (1.8)$$

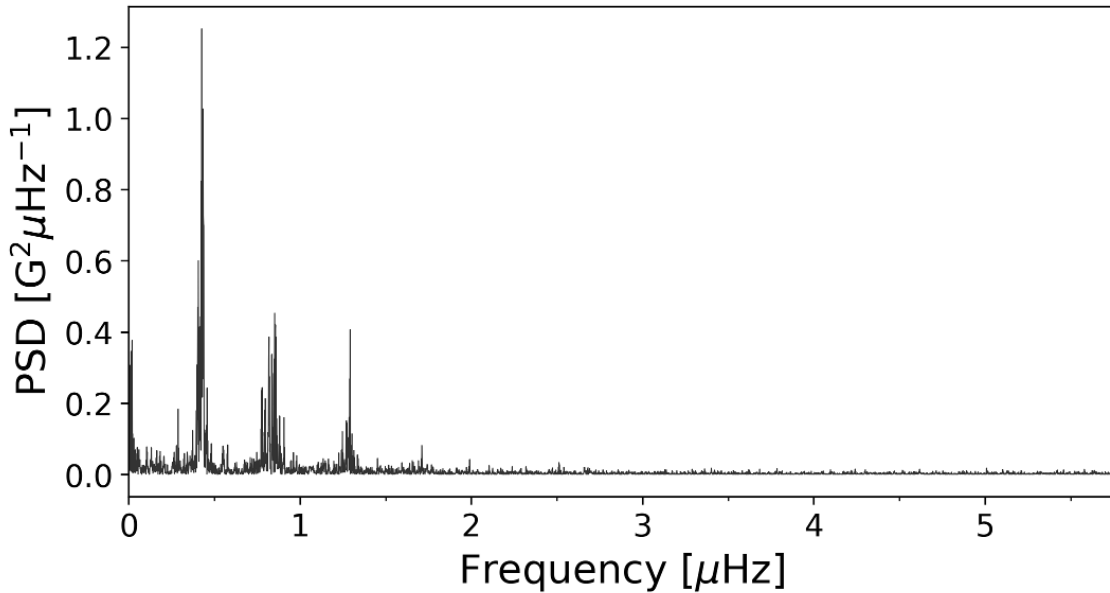
$$B(t) = \frac{1}{2} \left(\frac{d\mathcal{R}_{\text{calc}}}{dV} \right)^{-1} (\mathcal{R}_+ - \mathcal{R}_-) / K_B \quad (1.9)$$

Through the application of this methodology, one acquires the SMMF as shown

in Fig. (1.2a). The power spectrum of the SMMF is shown in Fig. (1.2b), and it shows a strong rotational signal at a period of ~ 27 days.



(a) BiSON SMMF 40-second cadence time series



(b) Power spectral density of the BiSON SMMF

Figure 1.2: (a) 40-second cadence observations of the SMMF from the Sutherland BiSON station between 1992 and 2012. The sense of the field was chosen to match the Chaplin et al. (2003) and the WSO observations, where positive is for a field pointing outwards from the Sun. (b) Power spectrum of the SMMF on a 40-second cadence truncated to 10 μ Hz, however the nyquist frequency is 12.5 mHz.

1.3.3 Comparison between WSO and BiSON

The relationship between the SMMF measured by the Sutherland BiSON station and the SMMF measured by the Stanford WSO was examined. The daily SMMF measured by the Stanford WSO and Sutherland BiSON station are plotted in Fig 1.3.

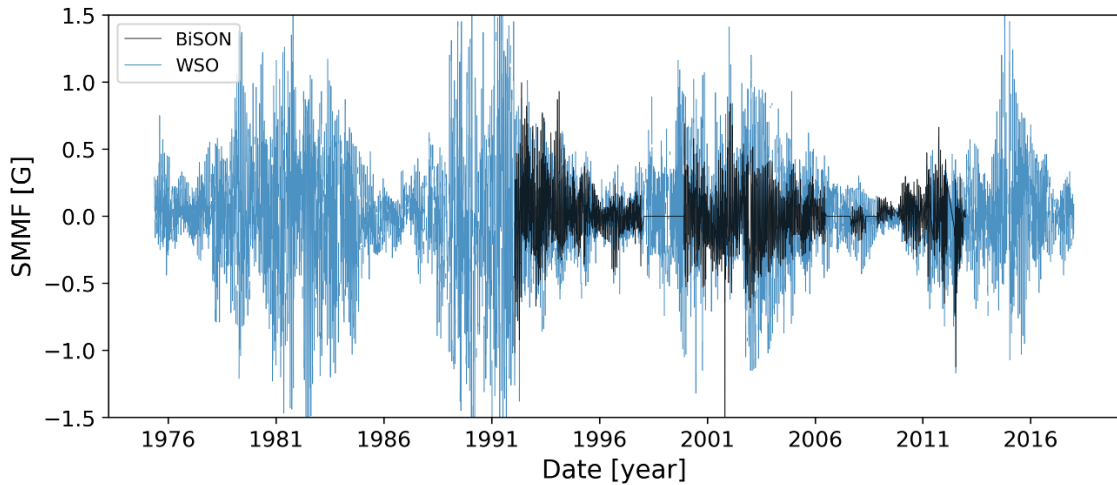


Figure 1.3: Daily averaged SMMF measured by WSO (blue) and by the Sutherland BiSON station (black).

Fig. 1.4 shows the correlation between the two data sets, and also a comparison of their power spectra at low frequencies. The gradient of the line in Fig. 1.4a is 0.4999 ± 0.0001 and informs us that the BiSON SMMF is half of the magnitude of that observed by WSO. ??...[This discrepancy may be due to the measurements of the SMMF using different spectral lines, hence their levels of formation in the solar atmosphere, and the divergence of magnetic field lines with altitude; an altitude difference of 100–200 km could lead to a difference of 30–50%.]...??

In addition, we can see quite clearly that the two power spectra align very closely, as shown in Fig. ??, and that both spectra appear to display an asymmetric peak shape, with a negative asymmetry.

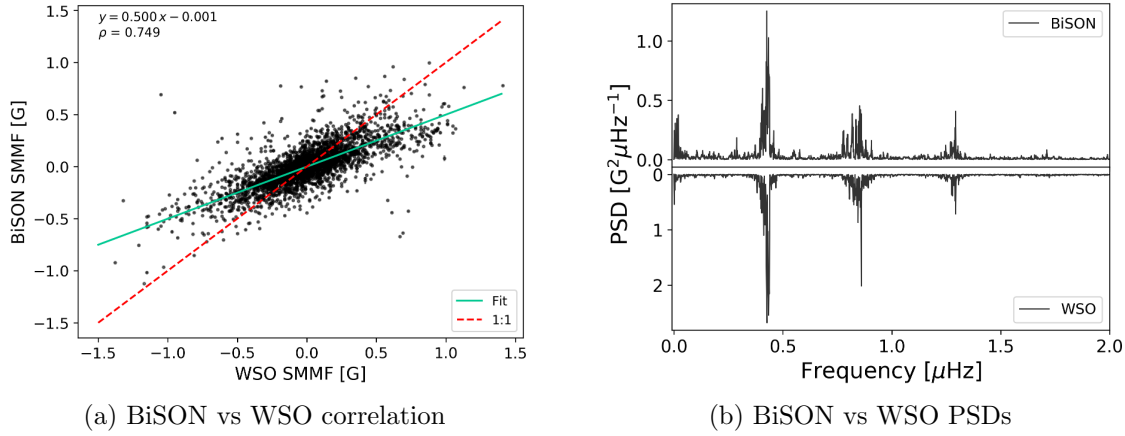


Figure 1.4: Comparisons between the BiSON SMMF data and the WSO SMMF data. (a) shows the correlation between daily averaged BiSON SMMF and the WSO SMMF. The green line provides the fit to the data, while the red line shows a 1:1 relation for comparison. (b) shows a comparison between the power spectra of BiSON and SMMF.

1.4 Methodology

1.4.1 Identifying Features in the SMMF Power Spectrum

The full power spectrum of the 40-second cadence SMMF is shown in Figure 1.5, covering a frequency range up to the Nyquist frequency of 12500 mHz, with a resolution of 1.516 nHz.

There are a number of features in the power spectrum. First, the peaks between $0.1 - 2.0 \mu\text{Hz}$ are a manifestation of a persistent rotational signal the SMMF. The distinct set of peaks indicates the existence of a long-lived, inhomogeneous, rotationally-modulated (RM) source. The SMMF signal exhibits a quasi-coherent nature in the time domain, and based on the comparatively short timescales for the emergence of magnetic features compared to their slow decay (Zwaan, 1981; Harvey & Zwaan, 1993; Hathaway & Choudhary, 2008), we assume the evolution of the RM component with time is a sudden appearance and a long, exponential decay.

As we have 40-second cadence observations of the SMMF, we were able to investigate the power spectrum up to a high Nyquist frequency. This was critical to uncovering a red-noise-like component in the power spectrum. This component

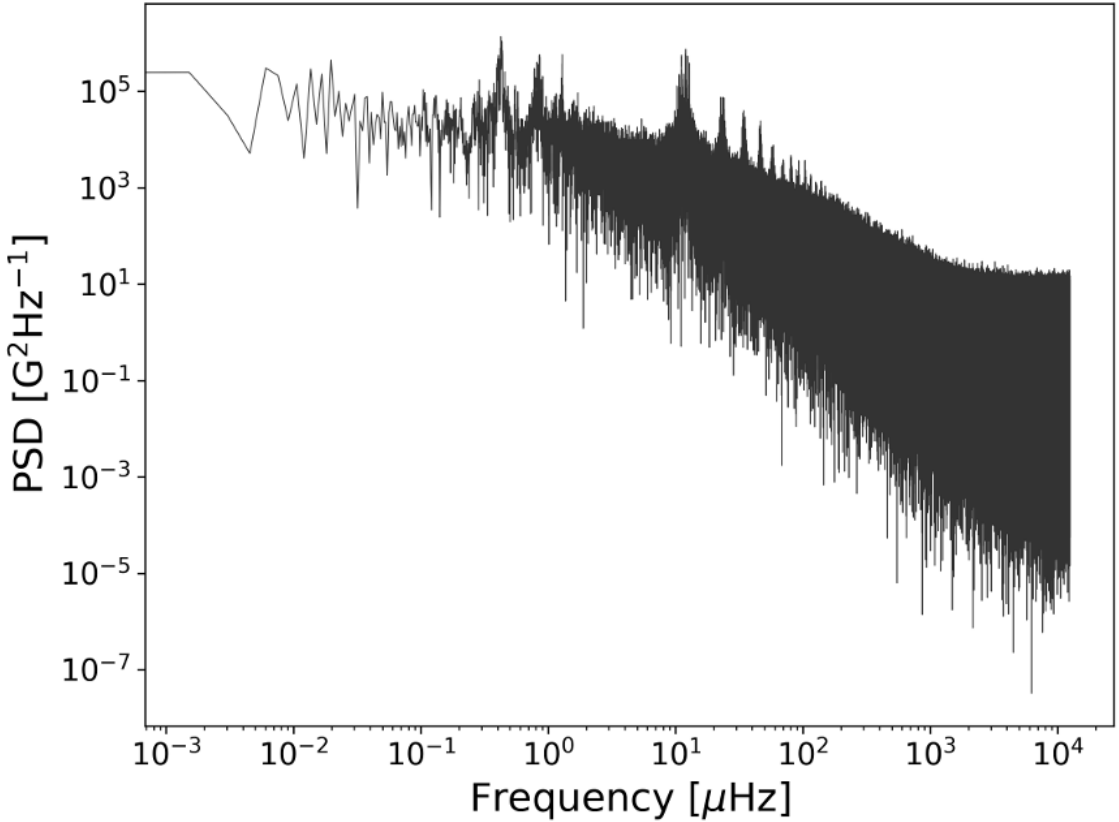


Figure 1.5: Full power spectrum of the BiSON SMMF on a logarithmic scale up to the Nyquist frequency.

could arise from continuously evolving, short-lived regions of magnetic field linked to magneto-convection, akin to a random walk, which we will dub the stochastic background (SB) component. Analogous to the SB is the granulation signal observed in the Doppler-velocity measurements of the solar surface (Basu & Chaplin, 2017).

In addition, at low-frequency, there is power associated instrumental noise and activity. At very-high frequency shot-noise is captured and sets the lower limit in power in the spectrum.

There are also side-band features in the power spectrum at multiples of 1/day $\sim 11.57\mu\text{Hz}$. The side-bands are a well-known phenomena in ground-based helioseismology. They arise from gaps in the data which are a consequence of making single-site, ground-based observations of the Sun.

The duty cycle of observations is very low, at around 15%, therefore it is also

important to take into consideration the effect that gaps in the data have on the power spectrum. Gaps in the data cause an aliasing of power from actual signal frequencies spread to other frequencies in the spectrum, and the nature of the aliasing depends on the properties of the window function of the observations. Hence before modelling the power spectrum the window function was well-characterised.

Understanding how the duty cycle of the observations affects the power spectrum we achieve will inform the way we parametrise the full model of the power spectrum.

1.4.2 Parameterisation of the SMMF Power Spectrum

In the frequency domain, each of the RM peaks models well as a Lorentzian distribution, similar to peak-bagging modes of solar oscillation (Handberg & Campante, 2011; Davies et al., 2014a), which is due to the quasi-coherent nature of the source. The exponential decay of the RM SMMF source gives width to the peaks in the power spectrum, which we can measure to infer their lifetime.

A single, symmetric Lorentzian peak can be modelled by equation (1.10), where ν is frequency, A_n is the mode amplitude of the RM component, Γ is the RM mode line-width, ν_n is RM mode frequency.

$$L_n(\nu; \Gamma, A_n, \nu_n) = \frac{2A_n^2}{\pi\Gamma} \left(1 + \left(\frac{\nu - \nu_n}{\Gamma/2} \right)^2 \right)^{-1} \quad (1.10)$$

Upon closer inspection of the power spectrum it is possible to see that the peak appear to exhibit an asymmetric shape, see Figure 1.2. Taking inspiration from (Howe et al., 2020), it is possible to allow for asymmetry in the Lorentzian peak, which is controlled by the asymmetry parameter, α , in equation (1.11):

$$L_n(\nu; \Gamma, A_n, \nu_n) = \frac{2A_n^2}{\pi\Gamma(\nu)} (1 + (2X(\nu))^2)^{-1} \quad (1.11)$$

where

$$X(\nu) = (\nu - \nu_n)/\Gamma(\nu) \quad (1.12)$$

$$\Gamma(\nu) = 2\Gamma/[1 + \exp^{-\alpha(\nu - \nu_n)}]. \quad (1.13)$$

In the limit where $\alpha \rightarrow 0$, we see that the asymmetric expression equates to the symmetric expression.

The model function used to describe the RM signal in the power spectrum is given by equation (1.14); the sum of N Lorentzian-peaks. The subscript, n , describes a single peak in the power spectrum; in implementing the model we constrain the mode frequencies such that they must be integer values of ν_0 : $\nu_n = n\nu_0$. This means that we define a single rotation frequency only, and subsequent peaks are harmonics. It is worth noting explicitly that this function assumes the line width of each Lorentzian peak is the same, only their amplitudes and central frequency differ.

When modelling the power spectrum we attempted with both the symmetric and asymmetric Lorentzian expressions, independently, to determine whether there is a necessity for the extra asymmetry parameter.

$$P(\nu) = \sum_{n=1}^N L_n(\nu; \Gamma, A_n, \nu_n) \quad (1.14)$$

Through this formulation we can measure the lifetime of the RM component (L), as it is related to the line-width of the peak by equation (1.15).

$$\Gamma = (\pi L)^{-1} \quad (1.15)$$

The low-frequency power can be incorporated into the model via the inclusion of a zero-frequency centred Lorentzian, i.e. Harvey-function, given by equation (1.16); where σ is the characteristic amplitude of the low frequency signal, and τ describes the characteristic timescale of the excursions around zero.

$$H(\nu; \sigma, \tau) = \frac{4\sigma^2\tau}{1 + (2\pi\nu\tau)^2} \quad (1.16)$$

The SB component can also be modelled using the Harvey-function, where σ is the characteristic amplitude of the red-noise signal and τ is its characteristic timescale.

The high frequency power is accounted for by the inclusion of a constant offset due to shot-noise, c .

1.4.3 Comparison with the WSO SMMF

To provide comparative results on the inferences from the BiSON SMMF, we repeated the analysis on the power spectrum of the WSO SMMF. The WSO data is however only sampled daily, hence the Nyquist frequency is lower than for BiSON, meaning a slightly different approach was taken.

The same parametrisation as outlined above was relevant to the modelling of the features in the WSO PSD, and the RM peak were fit using a model with symmetric Lorentzian peaks and separately with asymmetric Lorentzian peaks.

1.5 Results

1.5.1 Investigation of the Window Function

Daily gaps in the data cause some power from the low-frequency RM component in the power spectrum to be aliased to higher frequencies, specifically to harmonics of the frequency of the gaps in the data. In this case there are daily gaps, hence power is aliased to a frequency of $1/\text{day} \sim 11.57 \mu\text{Hz}$ and its harmonics.

As the mode frequency (and harmonics) of the RM component are located near zero ($\nu_0 \sim 0.4 \mu\text{Hz}$) there are negative and positive side-bands in the complete power spectrum, however we are usually only interested in positive frequencies. When considering the aliased power, both the positive and negative side-bands must be

taken into account. The aliased power is therefore located at frequencies defined in equation (1.17), where i denotes the side-band number, and n denotes the harmonic of the mode. The locations of side-bands are shown clearly to obey equation (1.17) in the SMMF power spectrum show in Fig. 1.6.

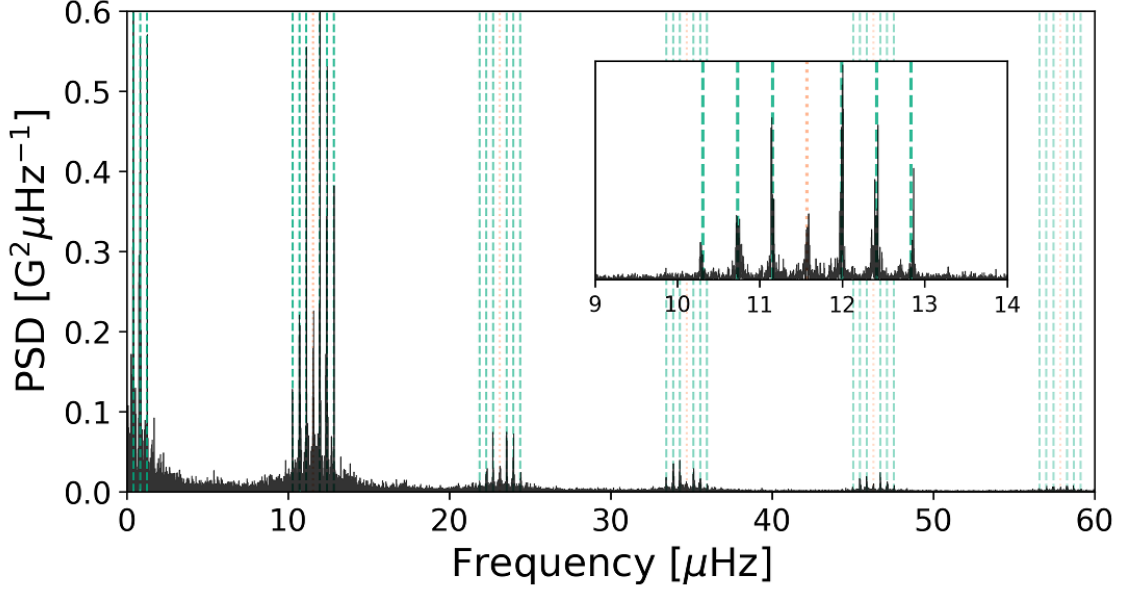


Figure 1.6: Locations of aliased power in side-band peaks. The orange dotted-lines show the locations of frequencies at multiples of 1/day. The green dashed-lines show the location of the side-band peaks – harmonic frequencies reflected around multiples of 1/day. The inset shows a zoom of one set of side-band peaks around 1/day.

$$\nu_{n,i} = i \left(\frac{1}{\text{day}} \pm \nu_n \right) \quad (1.17)$$

It is clear that we could therefore use the predicted locations of the aliased power and incorporate this into the model for the full power spectrum. This would however require us to explicitly model ~ 1100 groups of side-bands in order to cover this effect over the entire frequency range, and each group would require a unique parameter to control the fraction of power that is contributed to the full PSD. It can become computationally expensive to model each aliased peak and there is certainly room for degeneracy issues to occur.

An alternative approach is to utilise the power spectrum of the window function

itself. To do this the Fourier transform of the window function describing the duty cycle of observations was computed (i.e. $|\mathcal{F}[g(t)]|^2$), where the duty cycle function, $g(t)$, is given by equation (1.18).

$$g(t) = \begin{cases} 1 & \text{for } |B(t)| > 0 \\ 0 & \text{for } |B(t)| = 0 \end{cases} \quad (1.18)$$

To demonstrate the effect of the window function on the power spectrum, an artificial power spectrum was simulated with a single Lorentzian peak which followed equation (1.14), with parameter values. By computing the inverse Fourier transform, an artificial time-series was generated over the same epoch as the BiSON SMMF observations. We were then able to examine the effects of injecting gaps into the data which were concurrent with the BiSON SMMF gaps.

In Figure 1.7 the power spectrum of the window function is shown, as well as the noiseless input peak, and the output power spectra of the artificial data with and without the injected gaps. The power spectrum of the BiSON SMMF data is also plotted for comparison.

It is strikingly clear from Figure 1.7 that the shape of the spectrum of the window function has a remarkable resemblance to the BiSON SMMF spectrum and the output of the artificial spectrum with gaps injected. This shows that the periodic window function has a dominating effect on the power spectrum of the input signal which not only produces the diurnal sidebands, but also a broadband spread of the power.

Due to the broadband shape of the window function compared to the BiSON SMMF, it appears that there is actually no red-noise-like component in the SMMF and it is instead a manifestation of the gaps on the data. There does however still appear to be a necessity for a low-frequency Harvey function to describe the power close to zero

We can express the time series data ($y(t)$) as a multiplication of the signal ($f(t)$)

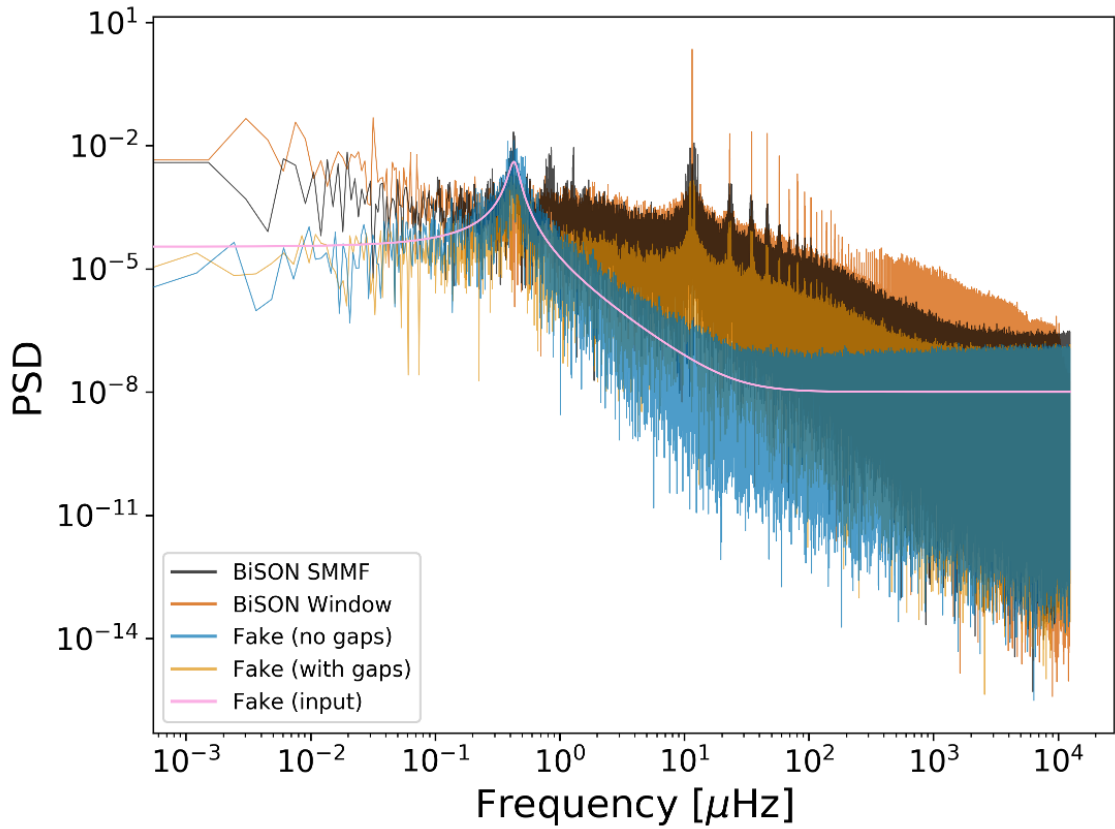


Figure 1.7: Shows the effects of the window function on the power spectrum. Black line: BiSON SMMF PSD; dark orange line: power spectrum of the window function; blue and light orange lines: the power spectrum of the artificial data without and with gaps, respectively; pink line: the input peak used to generate the artificial data.

with the window function ($g(t)$), as given by equation (1.19).

$$y(t) = f(t) g(t) \quad (1.19)$$

In the frequency domain, as the Fourier transform of a product becomes the convolution of the transformed components, it is possible to express the observed power spectrum in terms of the window function and the gap-free, model power spectrum, given in equation (1.20)

$$P'(\nu; \mathbf{a}) = P(\nu; \mathbf{a}) * |\mathcal{F}[g(t)]|^2 \quad (1.20)$$

Therefore to model the observed power spectrum in a robust manner, which

takes into account the intricacies caused by gaps in the data, we use a model which is formed of a model power spectrum, $P(\nu; \mathbf{a})$, convolved with the Fourier transform of the window function describing the duty cycle of observations ($|\mathcal{F}[g(t)]|^2$), i.e. a model described by equation (1.20), where

$$P(\nu; \mathbf{a}) = \sum_{n=1}^N L_n(\nu; \Gamma, A_n, \nu_n) + H(\nu; \sigma, \tau) + c. \quad (1.21)$$

Care was taken to ensure Parseval's theorem was obeyed, and no power was lost or gained from the convolution operation. The likelihood of the resulting model from the convolution, $P'(\nu; \mathbf{a})$, was then maximised to give the best fitting parameters.

1.5.2 Modelling the BiSON Power Spectrum

As there were many data points in the power spectrum, each likelihood computation was computationally expensive. In order to reduce the required computation, the power spectrum was mean re-binned by a factor of 3. As the power spectrum contained independent frequency bins, the χ^2 2-D.O.F likelihood function was used and we normalised the uncertainty in the model parameters from the posterior distributions, by dividing them by $\sqrt{3}$ (Appourchaux, 2003).

This likelihood evaluation doesn't fully take into account the correlated noise due to the convolution, however again due to the large quantity of data this would have required the computation of the determinant and inversion of a very large Toeplitz matrix, which would have been too expensive to compute; hence the pragmatic approach was to ignore this correlated noise in the likelihood calculation.

The mean re-sampled BiSON power spectrum was modelled against equation (1.20) (with $N = 4$ peaks) using the affine-invariant Markov Chain Monte Carlo (MCMC) sampler `emcee` (Foreman-Mackey et al., 2013) to explore the posterior parameter space.

The prior information on each of the parameters used during the MCMC sampling were uninformed uniform distributions (denoted by $\mathcal{U}(l, u)$ with l and u repre-

senting the lower and upper limits of the distribution respectively). The limits were set to cover a sensible range in parameter space, whilst limiting non-physical results or frequency aliasing.

$$\nu_0 \sim \mathcal{U}(0.38, 0.50) \mu\text{Hz}$$

$$\Gamma \sim \mathcal{U}(0.00, 0.11) \mu\text{Hz}$$

$$A_1 \sim \mathcal{U}(300, 900) \text{ mG}$$

$$A_2 \sim \mathcal{U}(100, 500) \text{ mG}$$

$$A_3 \sim \mathcal{U}(50, 350) \text{ mG}$$

$$A_4 \sim \mathcal{U}(20, 150) \text{ mG}$$

$$\sigma \sim \mathcal{U}(0.10, 1000) \text{ mG}$$

$$\tau \sim \mathcal{U}(0.10, 200) 10^6 \text{ s}$$

$$c \sim \mathcal{U}(10^{-2}, 10^2) \text{ G}^2 \text{ Hz}^{-1}$$

$$\alpha \sim \mathcal{U}(-500, 0)$$

In Table 1.1 the median values of marginalised posterior distributions for each of the model parameters of equation (1.20) are displayed. Reported uncertainties on the parameters correspond to the 1σ (68%) credible intervals either side of the median.

As the asymmetry parameter converged reasonably within the prior bounds we therefore deduce that the extra parameter was necessary, and the model utilising asymmetric Lorentzian peaks was a better fit to the data than the model with symmetric Lorentzian peaks.

The central frequency of this model, ν_0 implies a rotation period of $27.10^{+0.01}_{-0.01}$ days, and accounting for sidereal rotation, $25.23^{+0.01}_{-0.01}$ days. The rotation period measured

Table 1.1: Median values of the marginalised posterior distributions for each model parameter in the fit to the BiSON power spectrum. Numbers in brackets denote uncertainties on the last 2 digits, and all uncertainties correspond to the 68% credible intervals either side of the median.

Parameter	40-s symm.	40-s asymm.	Unit
ν_0	$0.42741^{(+15)}_{(-15)}$	$0.42761^{(+15)}_{(-15)}$	μHz
Γ	$0.03404^{(+67)}_{(-62)}$	$0.0471^{(+11)}_{(-10)}$	μHz
A_1	422.5 ± 1.9	$472.8^{+2.7}_{-2.8}$	mG
A_2	296.4 ± 2.3	343.8 ± 2.9	mG
A_3	209.9 ± 2.7	247.1 ± 3.1	mG
A_4	$78.9^{+4.2}_{-4.4}$	$101.0^{+4.7}_{-4.8}$	mG
τ	$62.1^{+4.7}_{-4.1}$	$84.4^{+6.8}_{-6.0}$	hours
σ	200.8 ± 3.2	183.3 ± 3.4	mG
c	$1.3411^{(+10)}_{(-10)}$	$1.3399^{(+10)}_{(-10)}$	G^2Hz^{-1}
α	—	$-134.6^{+5.4}_{-5.5}$	—

is in agreement with other literature for the rotation signal in the SMMF (Chaplin et al., 2003; Xie et al., 2017).

According to the model for differential rotation given by Snodgrass (1983) and Brown et al. (1989), the measured rotation period implies the RM component of the SMMF is sensitive to a time-averaged latitude of around 12° . This latitude is consistent with the latitudes spanned by sunspots and ARs over the solar activity cycle (Maunder, 1904; McIntosh et al., 2014; Thomas et al., 2019), and particularly during the declining phase of the solar cycle. This strongly implies that the origin of the RM component of the SMMF is linked to active regions of magnetic field.

Furthermore, from the measured line-width of the Lorentzian peaks, we have calculated the lifetime of the RM component using equation (1.15). The line-width suggests a RM lifetime of $78.2^{+1.8}_{-1.7}$ days, which is in the range 11 – 11.5 weeks. The typical lifetime of active magnetic regions and sunspots is usually on the order of weeks to months (Zwaan, 1981; Howard, 2001; Hathaway & Choudhary, 2008), therefore the observations of the SMMF by BiSON measure a lifetime of the RM component which is consistent with the lifetime of ARs and sunspots. This again suggests that the source of the signal is linked to active regions of magnetic field.

1.5.3 Comparison to the WSO Power Spectrum

A slightly different approach was taken when modelling the WSO power spectrum, compared to that applied to the BiSON PSD, due to the much lower Nyquist frequency. The duty cycle of the WSO observations over the same epoch as BiSON observations is $\sim 78\%$, therefore it was deduced that there is likely to be significantly less of a window effect in the observations; however despite this, a second Harvey function was introduced in order to account for any slight spreading out of power up to the Nyquist frequency.

The WSO PSD was modelled using equation 1.22, with $N = 3$, and $I = 2$

$$P(\nu; \mathbf{a}) = \sum_{n=1}^N L_n(\nu; \Gamma, A_n, \nu_n) + \sum_{i=1}^I H_i(\nu; \sigma_i, \tau_i) + c. \quad (1.22)$$

In Table 1.2 the median values of marginalised posterior distributions for each of the model parameters are displayed. Reported uncertainties on the parameters correspond to the 1σ (68%) credible intervals either side of the median.

Table 1.2: Median values of the marginalised posterior distributions for each model parameter in the fit to the WSO power spectrum. Numbers in brackets denote uncertainties on the last 2 digits, and all uncertainties correspond to the 68% credible intervals either side of the median.

Parameter	24-hr symm.	24-hr asymm.	Unit
ν_0	$0.42463^{(+44)}_{(-44)}$	$0.42736^{(+62)}_{(-64)}$	μHz
Γ	$0.0212^{(+16)}_{(-16)}$	$0.0198^{(+17)}_{(-16)}$	mG
A_1	$232.6^{+9.3}_{-8.9}$	$231.9 \pm .$	mG
A_2	$219.4^{+9.9}_{-9.0}$	$228.1 \pm .$	mG
A_3	$123.4^{+6.2}_{-6.0}$	$124.3^{+2.3}_{-2.2}$	mG
τ_1	$0.0725^{(+70)}_{(-67)}$	$0.0780^{(+63)}_{(-62)}$	10^6s
σ_1	$197.4^{+6.8}_{-6.4}$	$206.0^{+5.6}_{-5.3}$	mG
τ_2	$7.5^{+1.8}_{-1.4}$	$10.0^{+2.4}_{-1.9}$	10^6s
σ_2	$84.9^{+5.9}_{-5.5}$	$79.7^{+6.4}_{-5.7}$	mG
c	$2740.8^{+249.4}_{-283.7}$	$2662.2^{+224.9}_{-240.0}$	G^2Hz^{-1}
α	—	$-22.1^{+4.8}_{-5.5}$	—

1.6 Discussion

[To be included in here: discussion around the peak smearing affecting our ability to deduce the width and the source of peak asymmetry. This should be backed up by simulation results.]

1.6.1 Asymmetry in the Power Spectrum

We have shown that the BiSON and WSO SMMF power spectra are best modelled with asymmetric Lorentzian profiles. In this section, we investigate the cause of this asymmetry in the power spectrum.

An initial hypothesis on the origin of the asymmetry was the migration of active regions towards the equator with the progression of the solar cycle, this is illustrated by the clear asymmetry in the rotation frequency of latitudes sampled from a kernel density estimate of the SSN, in combination with models for the differential rotation (Snodgrass, 1983) and equatorial migration (Li et al., 2001a), shown in Figure 1.8. To investigate this as a source of the asymmetry, we used artificial data which was created to simulate the differential rotation and migration of active regions during the solar cycle. The methodology involved with generating the simulated data is discussed in Appendix A, and here we discuss the outcomes of the simulations.

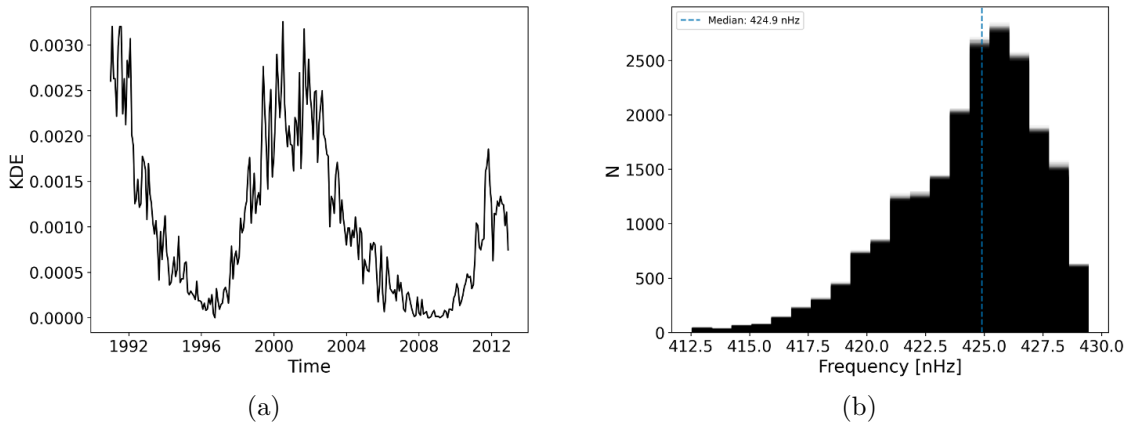


Figure 1.8: ...

Three separate models for the migration of ARs towards the equator were used

during the simulations and they are shown in Figure 1.9. The quadratic model was taken from Li et al. (2001a), which represents the ‘typical’ migration of ARs, and the linear and exponential models were parametrised to provided opposite extremes for a slower and faster migration towards the equator, respectively. The equations for each are given in equations (1.23), (1.24), and (1.25), where t is the time since cycle start in years.

$$\lambda_q = 0.0893t^2 - 2.8t + 27.24 \quad (1.23)$$

$$\lambda_l = -1.84t + 27.24 \quad (1.24)$$

$$\lambda_e = 20.24e^{-t/2} + 7 \quad (1.25)$$

The simulations were run with 15 configurations using the three migration models combined with models of sources (see Appendix A: cosine model), sign change model, and combinations of the cosine and sign change models in ratios of 5:95, 10:90, and 20:80). In each case, 250 simulations were run in order to produce a limit spectrum. Each limit spectrum was modelled with a series of Lorentzian peaks sharing a global asymmetry parameter, and the resultant asymmetries are shown in Figure 1.10.

It is immediately clear that the migration model has no significant effect on the asymmetry of the Lorentzian peaks, hence we are able to rule out AR migration as the origin of the asymmetry observed. This does however show an obvious difference between the way the different models of the sources have asymmetry manifested in their spectra.

This links to a still-open debate in helioseismology, on the source of asymmetry of the modes in the power spectra, and the asymmetry reversal between the observations in intensity and Doppler velocity. Asymmetry is regularly observed in p modes of oscillation in helioseismic data and we observe a difference in the sign of

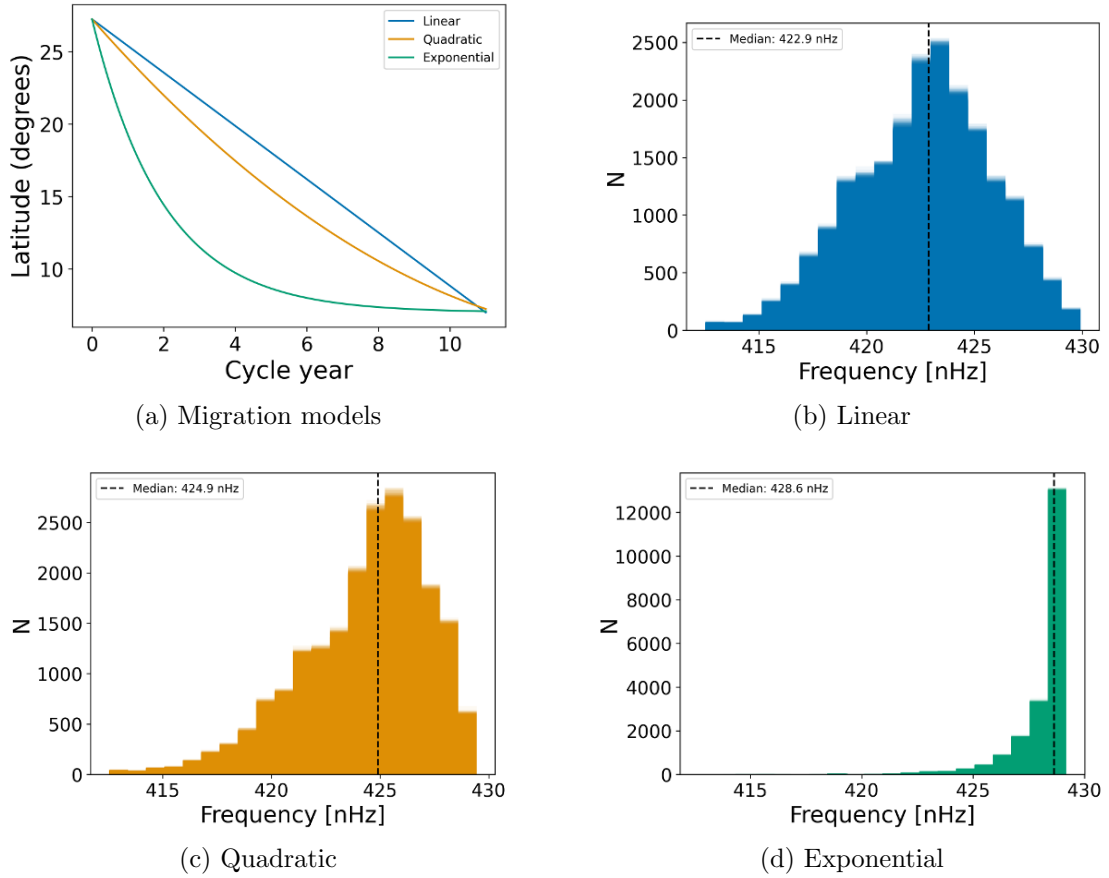


Figure 1.9: ...

the asymmetry term which is negative for Doppler velocity observations (i.e. more power in the low-frequency wing of the mode) and positive for measurements made in intensity (i.e. more power in the high-frequency wing of the mode) (Duvall et al., 1993; Chaplin & Appourchaux, 1999; Howe et al., 2015; Basu & Chaplin, 2017).

There are believed to be two main causes of asymmetry in acoustic modes:

1. The spatially localised nature of the excitation source of acoustic modes in the near-surface layers of the outer convection zone and the interference between concurrent waves that have been emitted by the an event but have traversed different paths before interfering, therefore accumulating phase difference between the waves. This source of asymmetry is believed to dominate in Doppler velocity observations.
2. The correlation between the convective granulation (i.e. correlated noise) and

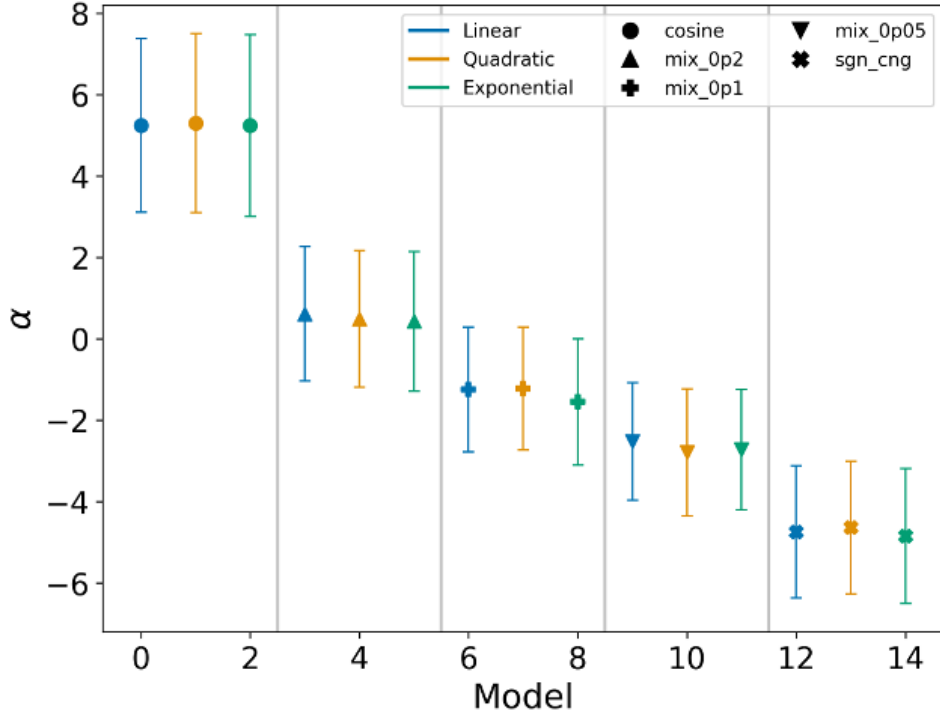


Figure 1.10: ...

the signal from the modes themselves, or the correlation between the excitations of one mode to another. This source of asymmetry is believed to dominate in intensity observations due to the lower signal-to-noise ratio.

We believe that some combination of phase difference between sources, and noise arising from some of the inevitable stochasticity in the simulations is responsible for the asymmetry difference observed between the cosine and sign change models, as they replicate the difference in the ways we observe the ARs, either by intensity (cosine model) or Doppler velocity (sign change model).

In the case of the SMMF observations, we believe the asymmetry is explained by the first of the above explanations. Active magnetic regions are typically localised in the near-surface layers of the Sun and we see clear interference between different regions of magnetic flux which form the observed more prominent active regions, which we believe contribute strongly to the SMMF. The interference between smaller regions of flux will likely have accumulated a phase difference and therefore could

contribute to the observed asymmetry.

On the second point, the SMMF is measured by the Zeeman splitting of an emission line due to the magnetic field, which is inherently a Doppler velocity method. There is no bleed through of p mode power in the spectrum and we have shown that there is no red-noise-like signal or stochastic background in the power spectrum, therefore it is unlikely that we see a strong correlated noise contribution to the asymmetry in the SMMF RM component peaks.

1.6.2 Testing the Effects of Differential Rotation and Active Region Migration

As a result of solar differential rotation and the migration of ARs towards the solar equator during the activity cycle, we know that the rotation period of ARs varies throughout the solar cycle.

As we have inferred that the RM component of the SMMF is likely linked to ARs, we may therefore assume that the RM component is also sensitive to migration. Here we analyse the effect of migration and differential rotation on our ability to make inferences on the lifetime of the RM component.

Several studies have modelled the the solar differential rotation, and its variation with latitude and radius of the Sun (see Beck (2000) and Howe (2009) for an in depth review of the literature on solar differential rotation). Magnetic features have been shown to be sensitive to rotation deeper than the photosphere; therefore in general magnetic features can be seen to rotate with a shorter period than the surface plasma (Howe, 2009).

Chaplin et al. (2008) analysed the effects of differential rotation on the shape of asteroseismic low- l p modes of oscillation, and showed that the consequence of differential rotation is to broaden the observed line-width of a mode peak. The authors provide a model of the resultant profile of a p mode whose frequency is shifted in time to be a time-average of several instantaneous Lorentzian profiles with

central frequency $\nu(t)$, given by equation (1.26). The angled brackets indicate an average over time, H and Γ are the mode height (maximum power spectral density) and line-width, respectively, and the full period of observation is given by T .

$$\langle P(\nu) \rangle = \frac{1}{T} \int_0^T H \left(1 + \left(\frac{\nu - \nu(t)}{\Gamma/2} \right)^2 \right)^{-1} dt \quad (1.26)$$

Chaplin et al. (2008) also show that by assuming a simple, linear variation of the unperturbed frequency, ν_0 , from the start to the end of the time-series by a total frequency shift $\Delta\nu$ (see equation (1.27)),

$$\nu(t) = \nu_0 + \Delta\nu \frac{t}{T} \quad (1.27)$$

the resultant profile of a p mode can analytically be modelled by equation (1.28):

$$\langle P(\nu) \rangle = \frac{H}{2\epsilon} \arctan \left(\frac{2\epsilon}{1 - \epsilon^2 + X^2} \right) \quad (1.28)$$

where ϵ and X are defined in equation 1.29 and equation 1.30.

$$\epsilon = \frac{\Delta\nu}{\Gamma} \quad (1.29)$$

$$X = \frac{\nu - [\nu_0 + (\Delta\nu/2)]}{\Gamma/2} \quad (1.30)$$

As the mode line-widths are broadened, we evaluate whether our ability to resolve the true line-width of the RM, and hence the lifetime, is affected. In order to evaluate this we computed the broadened profiles given by both equation (1.26) and equation (1.28), and fit the model for a single Lorentzian peak, to determine whether there is a notable difference in the line-width.

In the first instance, we compute the broadened peak using equation (1.26). Over the duration of the observations, we compute the daily instantaneous profile, $P(\nu(t))$. The time-averaged profile, $\langle P(\nu) \rangle$, is a weighted average of each instant-

taneous profile, where the weights are given by the squared-daily-SMMF, in order to allow a larger broadening contribution at times when the SMMF amplitude is greater.

In the second instance, we compute the broadened peak using equation (1.28). Over the duration of the observations the daily frequency shift is computed, $\Delta\nu$. The time-averaged shift, $\bar{\Delta}\nu$, is a weighted average, where again the weightings are given by the squared-daily-SMMF.

To determine the shift in the rotation rate as the active bands migrate to the solar equator, we used the model of the solar differential rotation as traced by magnetic features (Ω_m) given by equation (1.31), where $\mu = \cos\theta$ and θ is the co-latitude (Snodgrass, 1983; Brown et al., 1989).

$$\frac{\Omega_m}{2\pi} = 462 - 74\mu^2 - 53\mu^4 \text{ nHz} \quad (1.31)$$

The time-dependence on the latitude of the active regions used the best-fitting quadratic model by Li et al. (2001b).

In both instances, the broadened peak was modelled as a single Lorentzian peak using the first part of equation (??), i.e. the summation with $N = 0$. Again, we use `emcee` (Foreman-Mackey et al., 2013) to explore the posterior parameter space, priors similar to the above full-fit on the relevant parameters.

Over the entire duration of the SMMF observations, the time-averaged profile was calculated, using equation (1.26), and this is shown in Fig. 1.11a. The broadened mode used the input parameters outlined in Table ??, however with the background parameter set to zero.

By eye the broadened profile does not appear to have a significantly larger line-width. The input line-width was $0.047 \pm 0.001 \mu\text{Hz}$, and the fit to the time-averaged broadened peak produced a line-width of $0.047 \pm 0.005 \mu\text{Hz}$. The line-width of the broadened peak under this method is rather unchanged from that of the true peak, and both line-widths are within uncertainties of each other.

This result shows that numerically, the mode broadening effect of differential rotation and migration does not affect our ability to resolve the line-width of the peak, and hence the predicted lifetime of the RM component of the SMMF.

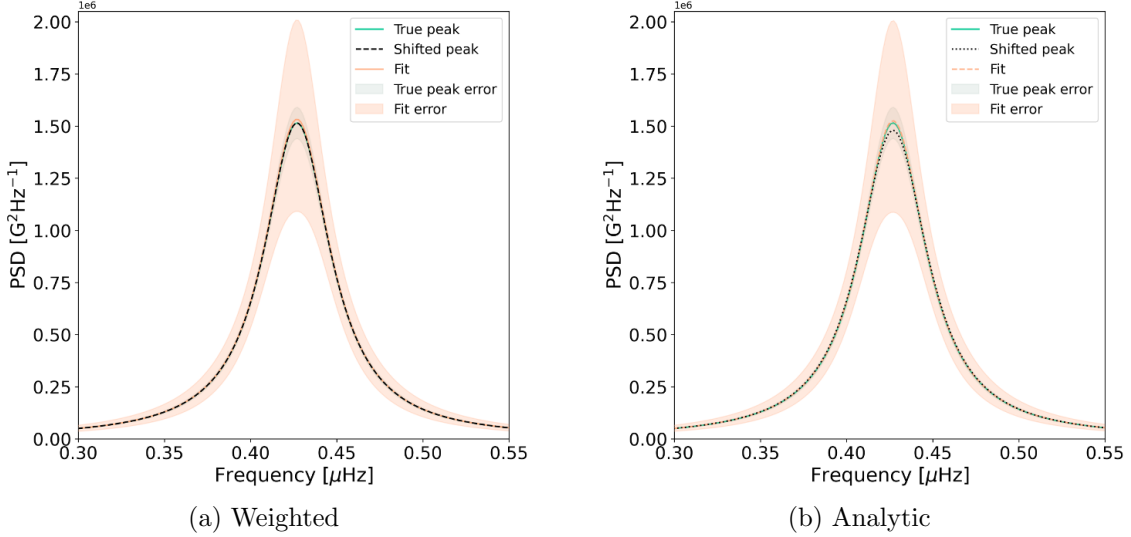


Figure 1.11: (a) Shows the peak distribution before and after the time-averaged broadening, and the fit to the broadened peak. (b) Shows the peak distribution before and after the analytical broadening, and the fit to the broadened peak. In both plots the broadened peaks have been shifted by the relevant frequency to overlay them on top of the true ν_0 for comparison.

The time-averaged frequency shift due to differential rotation was calculated, much in the same way as equation (1.26), to be $\Delta\nu = 0.01285 \mu\text{Hz}$. This shift was used to generate the broadened profile using equation (1.28). The broadened mode distribution also used the input parameters outlined in Table ??, however with the background parameter set to zero.

Similarly to the numerically broadened peak, by eye, the analytically broadened profile does not appear to have a significantly larger line-width and the resultant median parameters of the fitted Lorentzian profile are shown in Table ???. The input line-width was $0.047 \pm 0.001 \mu\text{Hz}$, and the line-width of the analytically broadened peak from the fit is $0.047 \pm 0.005 \mu\text{Hz}$, which is within the uncertainties of the line-width of the input peak.

This results shows that analytically, the mode broadening effect of differential

rotation and migration does not affect our ability to resolve the line-width of the peak, and hence the lifetime of the RM component of the SMMF.

Both broadening method applied have therefore been shown to have a negligible effect on the line-width of the profile, and our ability to resolve the true line-width of the peak remains unaffected. This result provides confidence that the measured line-width in Table ?? is the true line-width of the RM peaks, providing the correct life time for RM component, unaffected by migration and differential rotation.

1.6.3 Further Morphology of the SMMF

Here we use SDO/HMI data to show how the SMMF is broken down into its hemispheric behaviour and how that affects the full-disc SMMF...

1.6.4 Timescales in the SMMF

1.7 Conclusion

... ...

We leave the reader with the following points:

1. ...
2. ...
3. ...
4. ...

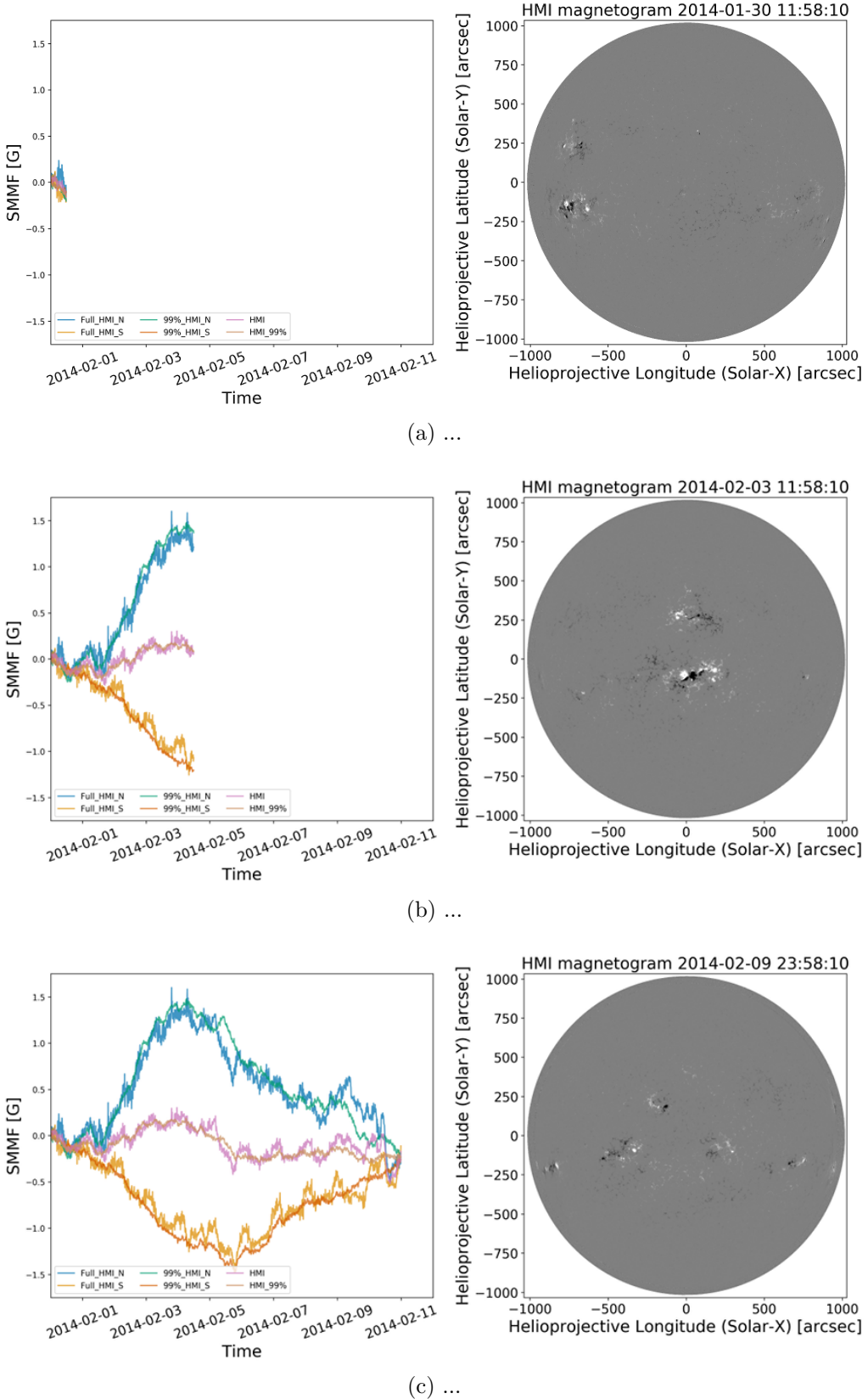


Figure 1.12: ...

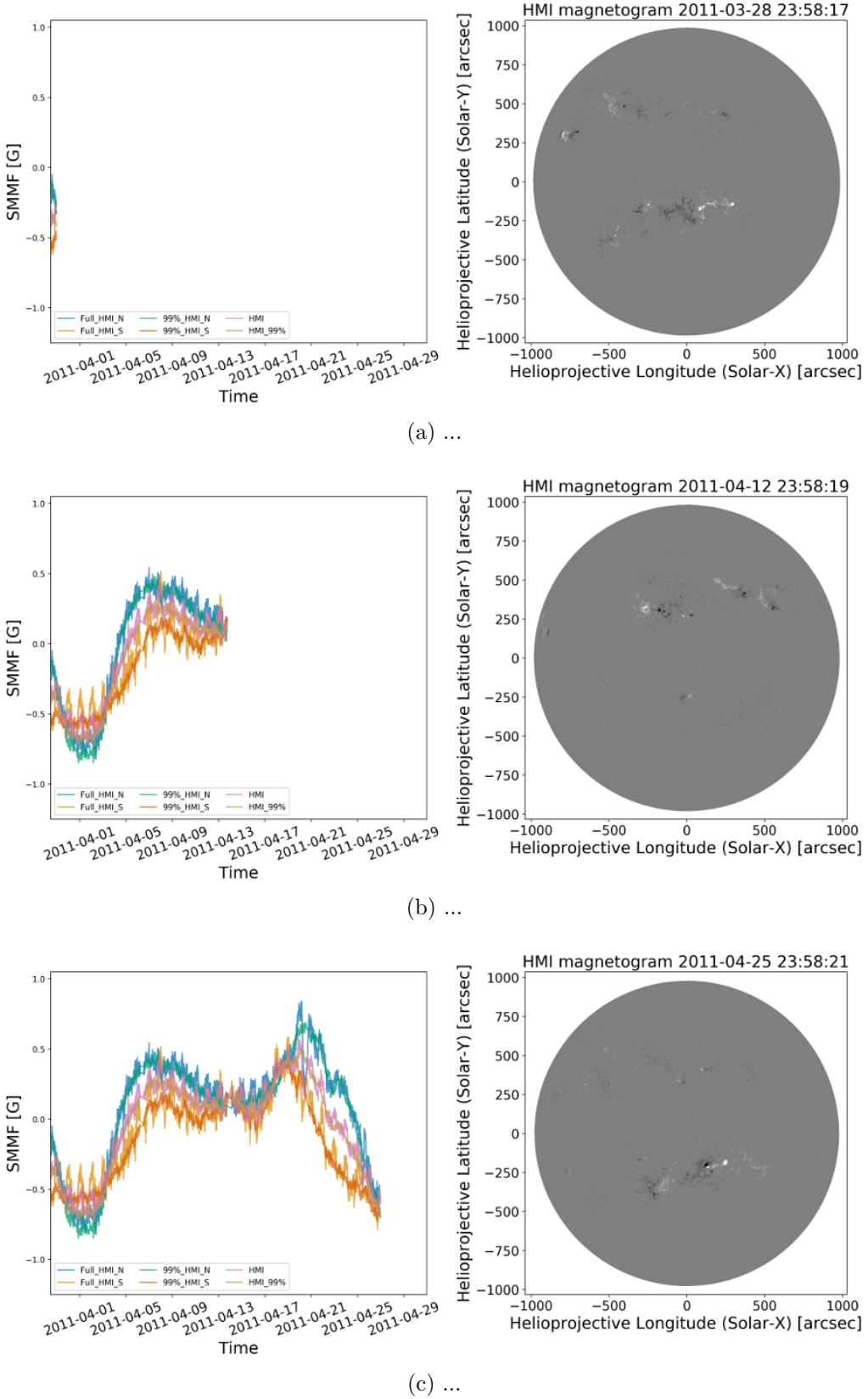


Figure 1.13: ...

2 Rossby Modes in the Solar Mean Magnetic Field

2.1 Introduction

Rossby waves, as first derived by Rossby & Collaborators (1939), have recently been discovered in the Sun through observations of near-surface flows by the Solar Dynamics Observatory Helioseismic and Magnetic Imager (SDO/HMI) (Löptien et al., 2018; Liang et al., 2019).

Rossby waves, or r modes, are toroidal modes of oscillation of a rotating, fluid body for which the dominant restoring force against the pressure gradients is the Coriolis force (Lanza et al., 2019; Hathaway & Upton, 2020). Rossby wave are associated with an undulation of a flow resulting in a pattern of radial vorticity of alternating sign. They are understood to form in the high atmosphere on Earth, heavily influencing global weather. For the Sun we observe that Rossby waves propagate in the retrograde direction, in the Carrington reference frame.

Recently, Löptien et al. (2018) provided an unambiguous detection of sectoral solar r modes by tracking the horizontal flows of granules in the solar photosphere during a 6-year period, using observations by SDO/HMI. Following this study Liang et al. (2019) confirmed the detection of solar r modes with time-distance helioseismology to measure deeper, subsurface flows in the meridional direction along the solar equator using both Solar and Heliospheric Observatory Michelson Doppler Im-

ager (SOHO/MDI) and SDO/HMI data, covering 21 years. In addition, Hanasoge & Mandal (2019) were also able to show the detection of solar r modes using a normal-mode coupling technique on 2 years of SDO/HMI data. In both of the observation conducted by Löptien et al. (2018) and Liang et al. (2019), the average lifetime of the r -modes were on the order of several months, and as long as a over a year for specific modes.

By monitoring the proper motions of solar supergranules using a local correlation tracking method Hathaway & Upton (2020) also report observing low latitude Rossby waves in full-disk Doppler images obtained by SDO/HMI, extending the measurements of Rossby waves to greater depths in the solar atmosphere, by an order of magnitude. The r modes observed have lifetimes which are only slightly longer than the Carrington rotation period, hence in slight disagreement with Löptien et al. (2018) and Liang et al. (2019), which Hathaway & Upton (2020) claim may be due the waves getting in and out of phase with each other as the low wave number waves propagate faster than the higher wave number waves. As these observations are at low latitudes, it is possible that they are linked to active magnetic regions and hence could be manifested in other sources of magnetic data.

Here we present the possible detection of the to-date unobserved, lowest frequency sectoral r mode using 21 years of BiSON observations of the line of sight (LOS) solar mean magnetic field (SMMF) (for details on the SMMF and BiSON, see Chaplin et al. (2003) and references within).

In an earlier study of the SMMF, the power spectrum of the BiSON observations was modelled using a combination of Lorentzian peaks and a convolution with the window function to account for the effect of gaps in the data. The full spectrum and the fit are shown in Figure 2.1.

We can divide through by the model, to achieve the residual spectrum, in which we have investigated and potentially found the signature of r modes. We find that although there exists a promising narrow-band region of significant power in the

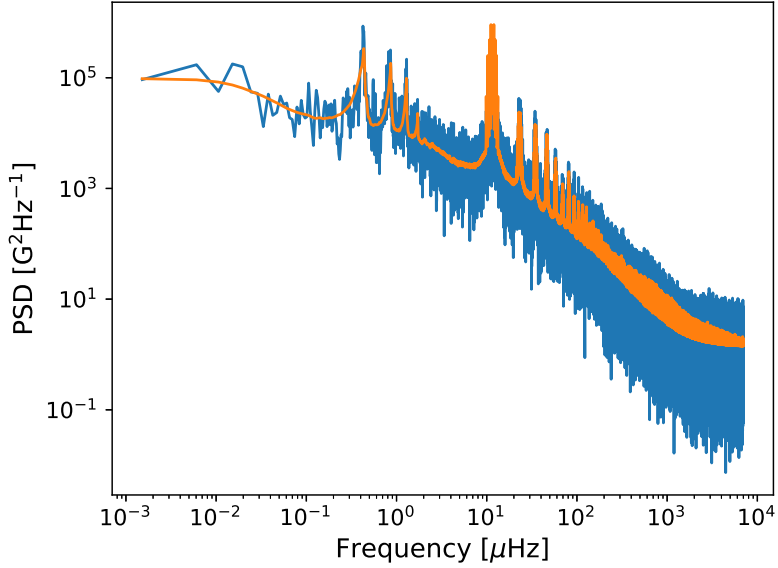


Figure 2.1: Model fit to the full BiSON SMMF PSD.

BiSON residuals spectrum, which could be the $l = m = 2$ mode, the r mode does not exist in other sources of SMMF data, hence the observed peak is more likely explained as being a source of prominent noise in the BiSON observations.

2.2 Aims

In this chapter the residual power spectrum of the BiSON SMMF, after removing a model for the dominant signal, was investigated in order to search for the existence of r-modes. Within the residual spectrum we test for the existence of r modes and where they appear to exist, a Lorentzian model is fit to understand the properties of the source.

Further analysis is provided using simulated data to better understand how an annual modulation of the r mode observations would affect their frequencies. In addition, SDO/HMI data is investigated to support the argument that r modes are not split in the power spectrum and instead we should observe the central frequency and lower amplitude side bands.

2.3 Theory

The detailed theory of the effect of r modes on observational data was re-visited recently by Lanza et al. (2019) in light of the solar observations, in an effort to determine the effect on radial velocity detections of exoplanets.

Under the assumption of a slow, uniformly rotating sphere (with angular velocity, Ω , where $\Omega^2 \ll GMR^{-3}$), the frequencies of global r modes in the Carrington rotating frame is well approximated by eq. (2.1), where $l > 0$ is the angular degree and m is the azimuthal order (Löptien et al., 2018; Lanza et al., 2019).

$$\nu_{carr} = -\frac{2m\Omega}{l(l+1)} \quad (2.1)$$

In an inertial frame the observed r-mode frequencies will be (Lanza et al., 2019):

$$\nu_{in}(l, m) \approx m\Omega - \frac{2m\Omega}{l(l+1)} = m\Omega \left(1 - \frac{2}{l(l+1)}\right) \quad (2.2)$$

where Ω is the mean sidereal rotation rate, and l and m are the angular and azimuthal degree, respectively. Sectoral Rossby waves are obtained by setting $l = m$ in this equation. A consequence is that they propagate with a retrograde phase velocity as $\nu/m = -2\Omega/[m(m+1)] < 0$.

An Earth-based observer, orbiting the sun, shall expect to observe frequencies adjusted by the orbital frequency, $\nu_{\oplus} \approx 31.7\text{nHz}$, given by equation (2.3).

$$\nu_{obs}(l, m) = \nu_{in}(l, m) - m\nu_{\oplus} \quad (2.3)$$

In addition, due to the tilt of the ecliptic with respect to the solar equatorial plane (the solar B_0 angle), the visibility of the modes will vary on a time-scale of 1–yr, meaning we expect to actually observe split peaks at frequencies of $\nu_{obs}(l, m) \pm \nu_{\oplus}$ (Lanza et al., 2019)).

Based on this theory, we can compare the observed sectoral r modes with those

predicted. These frequencies are summarised in Table 2.1.

Table 2.1: Predicted⁺ and observed[◦] r mode frequencies for combinations of l and m . Predicted frequencies and conversions of observations to different frames of reference use equation (2.1), equation (2.2), and equation (2.3), with $\Omega = 453.1$ nHz. The predicted splitting for the B_0 angle variation is also provided. The key for the source column is: LPT for Löptien et al. (2018), LNG for Liang et al. (2019), and LZA for Lanza et al. (2019).

Frequency	Source	$l = m = 2$	$l = m = 3$	$l = m = 4$	$l = m = 5$
ν_{carr} [nHz]	LPT [◦]	–	-259	-194	-157
	LNG [◦]	–	-253	-198	-156
	LZA ⁺	-302.1	-226.6	-181.2	-151.0
ν_{in} [nHz]	LPT	–	1100	1618	2109
	LNG	–	1106	1614	2110
	LZA	604.1	1132.8	1631.2	2114.5
ν_{obs} [nHz]	LPT	–	1005.2	1491.7	1950.1
	LNG	–	1011.2	1487.7	1951.1
	LZA	540.8	1037.7	1504.4	1956.0
$\nu_{obs} + \nu_{\oplus}$ [nHz]	LPT	–	1036.9	1523.3	1981.8
	LNG	–	1042.9	1519.3	1982.8
	LZA	572.4	1069.4	1536.1	1987.7
$\nu_{obs} - \nu_{\oplus}$ [nHz]	LPT	–	973.6	1460.0	1918.4
	LNG	–	979.6	1456.0	1919.4
	LZA	509.1	1006.0	1472.7	1924.3

2.4 Methodology

2.4.1 Testing the Residual Spectrum

In order to investigate the presence of Rossby wave modes in the power spectrum of the BiSON SMMF, statistical significance tests were employed using a false-alarm approach, to test the probability of finding prominent narrow-band power in the residual spectrum.

We assume negative exponential statistics (i.e. χ^2 2-degrees of freedom distribution), and that the bins in the power spectrum are uncorrelated (an assumption which may be incorrect due to the low fill-factor of the BiSON SMMF data). Then we can find the false alarm probability, or probability to observe power in a given frequency bin, ν , that is greater than or equal to a given threshold.

The probability to observe power in a given frequency bin, ν , that is greater than or equal to $P(\nu)$ is:

$$p[P(\nu)] = \frac{1}{P_{lim}(\nu)} \exp\left(-\frac{P(\nu)}{P_{lim}(\nu)}\right) \text{ or; } p[P(\nu)] = \frac{1}{\langle P(\nu) \rangle} \exp\left(-\frac{P(\nu)}{\langle P(\nu) \rangle}\right), \quad (2.4)$$

where $P_{lim}(\nu)$ is the limit spectrum or $\langle P(\nu) \rangle$ is a well-fitting model/estimate to the spectrum. Considering a relative power approach (i.e. considering the power relative to the mean level or model of the PSD), equation (2.4) may be written more concisely as:

$$p(s_\nu) = e^{(-s_\nu)}, \quad (2.5)$$

where,

$$s_\nu = P(\nu)/\langle P(\nu) \rangle, \quad (2.6)$$

and $\langle P(\nu) \rangle$ is reduced to 1 when we compare the power relative to the power spectrum residuals.

In reality, we use the χ^2 cumulative distribution function to compute the probability of power, which is given by equation (2.7), where k is the number of degrees of freedom, $\gamma(s, t)$ is the lower incomplete gamma function and $P(s, t)$ is the regularized gamma function.

$$F(x; k) = \frac{\gamma(\frac{k}{2}, \frac{x}{2})}{\Gamma(\frac{k}{2})} = P\left(\frac{k}{2}, \frac{x}{2}\right) \quad (2.7)$$

Using these expressions, we can rewrite the equation for $P(s_\nu)$ as given by equation (2.8). This allows us to compute the probability of statistically significant peaks in the residuals for re-binned data.

$$p(s_\nu) = 1 - F(2s_\nu; k) = 1 - P\left(\frac{k}{2}, s_\nu\right) \quad (2.8)$$

The probability that a bin has power at or above the level s_ν is therefore given by equation (2.5), or more generally by equation (2.8), hence the probability that we fail to find a bin with power at or above the level s_ν is $1 - p(s_\nu)$; thus the probability of failing to find a bin with power at or above s_ν in N -bins in the spectrum is $[1 - p(s_\nu)]^N$. Therefore the probability to find at least one bin with power at or above s_ν in N -bins in the spectrum is:

$$p_N = 1 - [1 - p(s_\nu)]^N \quad (2.9)$$

where a low value for p_N indicates that the spike in power in that bin is unlikely to be a statistical fluctuation, and therefore is considered a statistically significant spike.

This can be generalised using the cumulative binomial distribution. The probability of finding at least r spikes in N -bins at or above the relative power level s_ν is given by equation (2.10), which is equal to equation (2.9) when $r = 1$.

$$p[r; p(s_\nu), N] = 1 - Pr(X < s_\nu) = \sum_{r=r}^N \binom{N}{r} p(s_\nu)^r [1 - p(s_\nu)]^{N-r} \quad (2.10)$$

By applying equation (2.10) to the residuals of in the power spectrum, we can test whether there are any significant peaks in the residual power spectrum. Again, a low value for $p[r; p(s_\nu), N]$ indicates that the power in that bin is unlikely to be a statistical fluctuation.

2.4.2 Modelling r mode Profiles

In the location of any suspected r modes in the residual spectrum, we can model the profile of the peak by using a Lorentzian distribution, using the form expressed

by eq. (2.11), where A is the amplitude of the signal, Γ is the line width of the distribution, and ν_0 is the central frequency of the distribution. This follows the methodology adopted by Löptien et al. (2018) and Liang et al. (2019).

$$P(\nu) = \frac{2A^2/(\pi\Gamma)}{1 + (2(\nu - \nu_0)/\Gamma)^2} \quad (2.11)$$

Modelling was performed using the `pymc3` No U-Turn Sampler (NUTS) extension to a Hamiltonian Monte Carlo (HMC) sampling algorithm (Salvatier et al., 2016).

2.5 Results

2.5.1 Testing the Residual Spectrum

The residual spectrum is shown in Figure 2.2, with the removed model and locations of r mode frequencies predicted by Lanza et al. (2019) over-plotted.

It is clear from Figure 2.2 that there appears to be a resolved peak of narrow-band power in both the location of the $l = m = 2$ r mode and perhaps also the upper B_0 -variation-modulated $l = m = 3$ r mode.

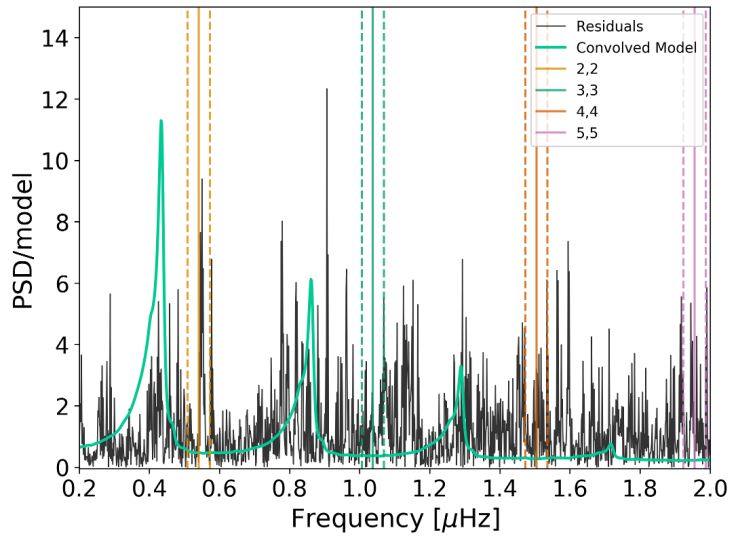


Figure 2.2: Residual power spectrum of the BiSON SMMF. Over plotted in the green curve is the model of the main SMMF signal. Also over plotted as vertical solid lines are the expected locations of the 4 lowest-frequency sectoral r modes and the dashed lines, the locations of the B_0 variation frequency splitting.

Table 2.2: Median posterior values of the Lorentzian model for the r -mode peak in the BiSON SMMF PSD residuals. Numbers in brackets denote uncertainties on the last 2 digits, and all uncertainties correspond to the 68% credible intervals either side of the median.

Parameter	Value	Unit
ν_0	$0.5500^{(+16)}_{(-16)}$	μHz
Γ	$0.0057^{(+47)}_{(-29)}$	μHz
A	$0.253^{+0.066}_{-0.050}$	—
<i>bgnd</i>	0.99 ± 0.16	—

The statistics tests were performed on the residual spectrum for various re-binning factors, n . The plots summarising the statistics tests are shown in Fig. 2.3 for re-binning factors of $n = 1, 2, 5$, and 10 .

These tests suggest that the feature around $0.5 \mu\text{Hz}$ may be a signal related to r modes, as its location is roughly correct for the $l = m = 2$ mode consistently has a low false alarm (FA) probability. The other low FA probability features tend to be associated with the residuals from the main harmonics of the SMMF signal, and are the result of a slight failing of the main model of the power spectrum.

In particular in Figure 2.3b, there is compelling evidence to suggest that this peak is significant. In order to solidify this conjecture, we aimed to fit a model to the residuals around this peak in order to confirm whether the properties of the peak resembled those suggested by Löptien et al. (2018), Liang et al. (2019), and Lanza et al. (2019).

2.5.2 Modelling r mode Profiles

Using the model for the Lorentzian peak (eq. 2.11), we modelled the residual spectrum around the location of the potential $l = m = 2$ mode. The results of the fit are given in Table 2.2 and the fit to the residuals is shown in Figure 2.4.

The median of the posterior distribution for the width parameter suggests an e-folding lifetime ($1/(\pi\Gamma)$) of around 650 days (~ 1.8 years), which follows the order magnitude of the lifetime suggested by low- m Rossby modes. The lowest r mode

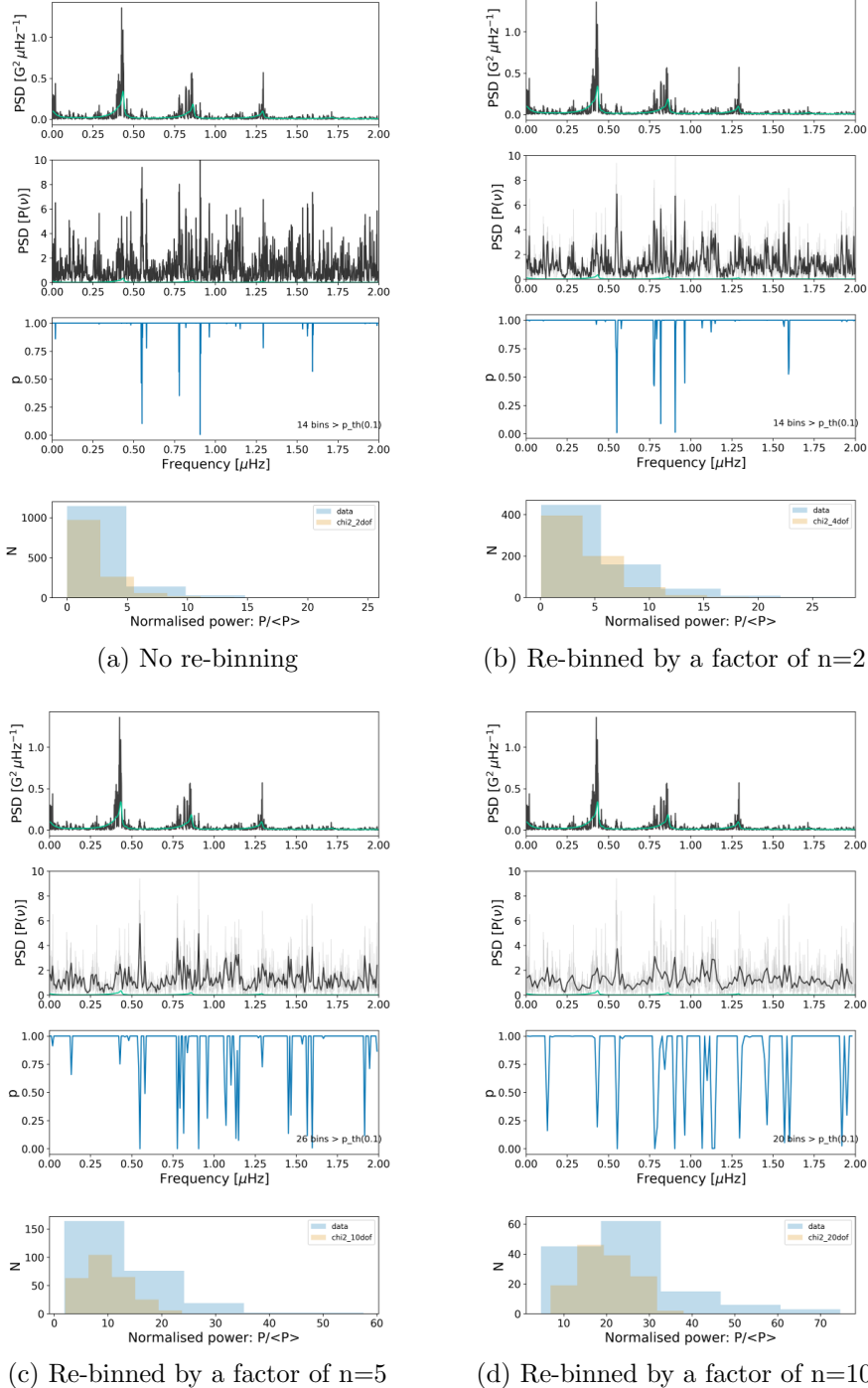


Figure 2.3: Realisations of the statistics tests of BiSON data for different re-binning factors (n). The panels of each sub figure are: (top) the full PSD and fit, (second panel) the full and re-binned residuals, (third panel) the probability of statistical noise in each bin, (bottom) distribution of the residuals compared to a χ^2 $2n$ -DOF.

observed, $l = m = 3$, was shown to exhibit a lifetime of over a year (~ 1.4 years) by Liang et al. (2019). The $l = m = 4$ were observed by both Löptien et al. (2018) and

Liang et al. (2019) to have a lifetime of ~ 0.6 years and ~ 0.3 years, respectively. There seems to be a slight increasing trend in the mode lifetimes observed by Löptien et al. (2018) and Liang et al. (2019) of longer lifetimes for lower m , therefore the long lifetime found here for the $l = m = 2$ mode is entirely reasonable and in-line with current observations.

The model of the mode in the residuals spectrum has a magnetic amplitude of ~ 29 mG, which equates to a radial velocity amplitude of $\sim 8.4 \text{ cm}^{-1}$. Lanza et al. (2019) state that the maximum RV amplitude of the $l = m = 2$ mode is $\sim 24.5 \text{ cm}^{-1}$, meaning our observed peak is around a third of the maximum RV amplitude one might have expected to observe. This is however an upper limit given by Lanza et al. (2019), and therefore the lower amplitude in the model should not be concerning.

In particular, however, we can see that the background is ~ 1 , which is expected for such a fit to residual PSD data. Due to the accuracy of the background, the agreement between the central frequency of the fit to the $l = m = 2$ mode, the agreement in the order of magnitude of the e-folding lifetime, and the amplitude of the mode residing below the upper limit suggested by Lanza et al. (2019), we believe there is strong evidence to suggest that this peak, which has shown to be significant through the false-alarm statistics tests, is the $l = m = 2$ sectoral r mode, observed in the BiSON SMMF data.

2.6 Discussion

Despite the compelling results presented in the previous section there remained an open question on the way the Rossby waves would manifest themselves in the power spectrum. The BiSON power spectrum was also compared to the power spectra of the WSO SMMF and the SDO/HMI SMMF to cross-reference the finding.

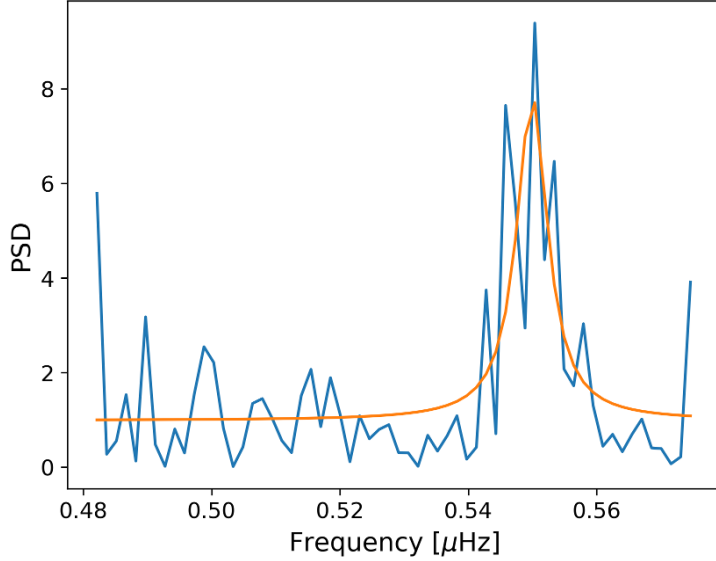


Figure 2.4: Model fit to the r mode in the BiSON PSD residuals using the median from the parameter posterior distributions.

2.6.1 Manifestation of Rossby Waves in the Power Spectrum

It was suggested by Lanza et al. (2019) that the mode should be split into two frequencies due to the annual variation of the B_0 angle, but the observed peak in the BiSON spectrum is located at approximately the location of the central frequency; therefore the observation is not split due to this modulation. We needed to determine if this was physically observable.

Figure 2.5 shows a schematic diagram of the flow of a $l = 2 = m$ sectoral r mode. One can clearly see from the more visible purple region of the schematic, the Southern Hemisphere flow is oriented out of the page, whereas the Northern Hemisphere flow is oriented into the page. Due to the B_0 modulation, a varying of the sign of the flow would be observed over this region, i.e the velocity of the flow. In the more red-green regions the schematic, the flow is more transverse, hence this would contribute less to the effect of the B_0 modulation.

We needed to therefore understand whether the SMMF observations have a hemispheric dependence that would lead to a change sign in the observations due to the

B_0 variation. In addition, this raised the question of how the mode was affected in the power spectrum by the B_0 modulation; either split into separate peaks as suggested by Lanza et al. (2019) or instead was it possible that we could have a situation where the mode at the central frequency remained?

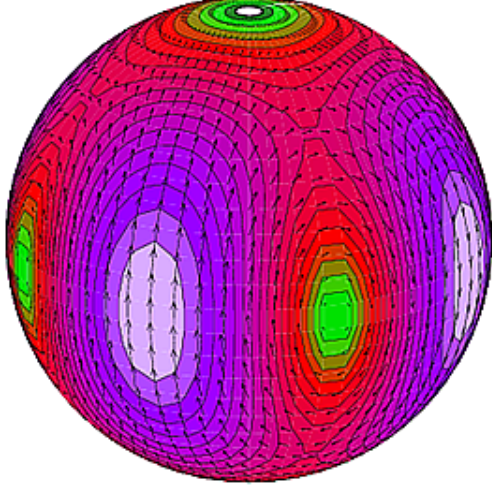


Figure 2.5: Mode displacement schematic for an $l = m = 2$ r mode (Strohmayer & Mahmoodifar, 2014)

To investigate the splitting of the mode, a simple model was produced whereby a sinusoid function (with a period of ~ 25 days) was modulated by either a cosine or rectified cosine function (with a period of 1 year). In the former, using the cosine modulation, this represents observing the sign of the flow varying with the B_0 modulation. Conversely in the latter simulation, this instead represents a variation of the amplitude, and it does not change the sign. Figure 2.6 shows the time series of the two cases to more clearly show their difference. The power spectrum of each case was then computed and these are shown in Figure 2.7 to demonstrate the differences between the modes produced.

One can clearly see the difference in the power spectrum produced in each of the cases. In the velocity modulation case, we see a splitting of the oscillation mode into two peaks split around the expected mode frequency by $\pm\nu_{\oplus}$. There exists no more power at the central mode frequency in this case and is in agreement with the scenario suggested by Lanza et al. (2019). In the amplitude modulation case, we see

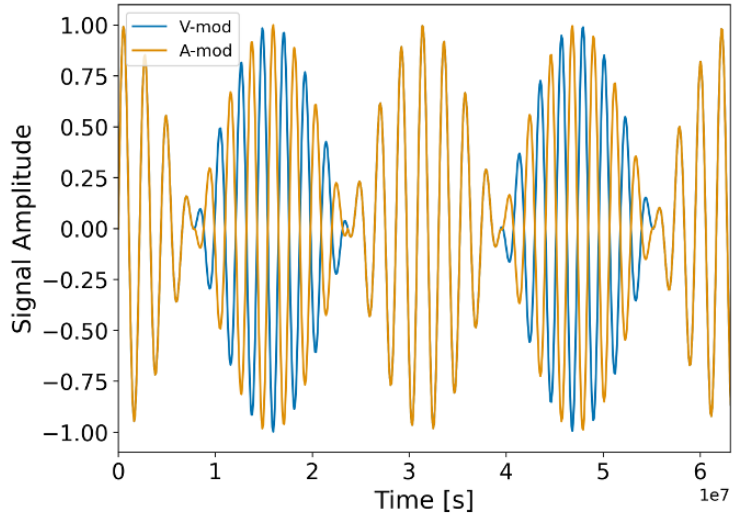


Figure 2.6: Time series of the velocity and amplitude modulation toy model simulations. The blue curve shows the velocity modulation, i.e. modulating using a cosine with period 1 year, whereas the orange curve shows the amplitude modulation, i.e. modulating using a rectified cosine with period 1 year.

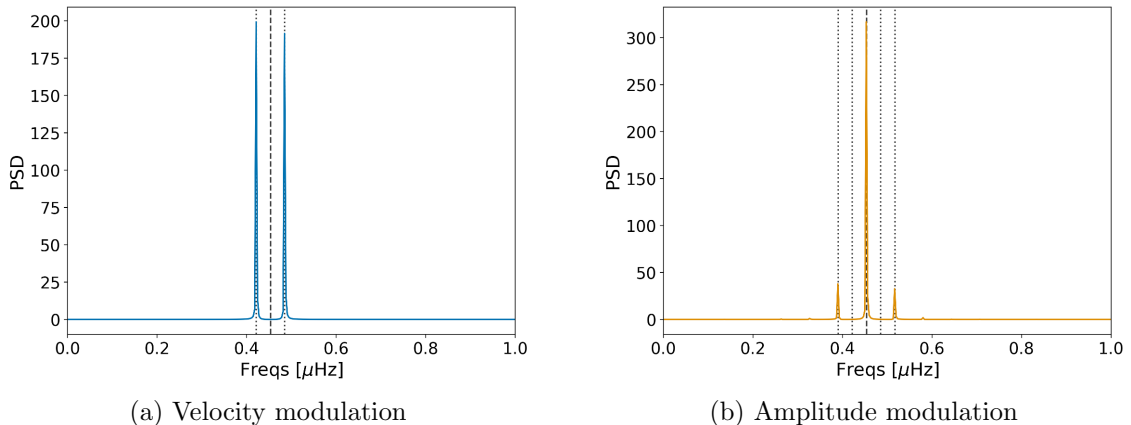


Figure 2.7: Power spectra for the two modulation methods, showing the difference in the way the modulation has changed the frequency of the observed mode.

a production of sidebands at $\pm 2\nu_{\oplus}$ however the expected mode frequency remains in this scenario and has a significantly higher peak height, a ratio of 90:10 in favour of the central peak.

We have shown that it is possible to retain the central frequency of the r mode in the power spectrum if the B_0 modulates the amplitude of the observations and not the sign. With this known, it was then necessary to understand whether the two hemispheres of the Sun contribute signals that are more analogous with the

velocity modulation or amplitude modulation. In the former, velocity modulation, we would expect to see a persistent anti-correlation between the two hemispheres. In the latter, amplitude modulation, we would expect to see the signals from each hemisphere that are correlated, which track each other and which can be both positive or negative.

We can investigate how the two hemispheres of the Sun contribute to the SMMF through analysis of SDO/HMI data. To do this, we acquired 720s-cadence magnetograms from SDO/HMI using the `SunPy` python module (Barnes et al., 2020) for the rising phase of solar cycle 24 during 2011, and for the maximum of cycle 24 during 2014. It was possible to separately average the Northern and Southern Hemispheres' contributions to the total, disk-averaged SMMF. The plot of this data is shown in Figure 2.8.

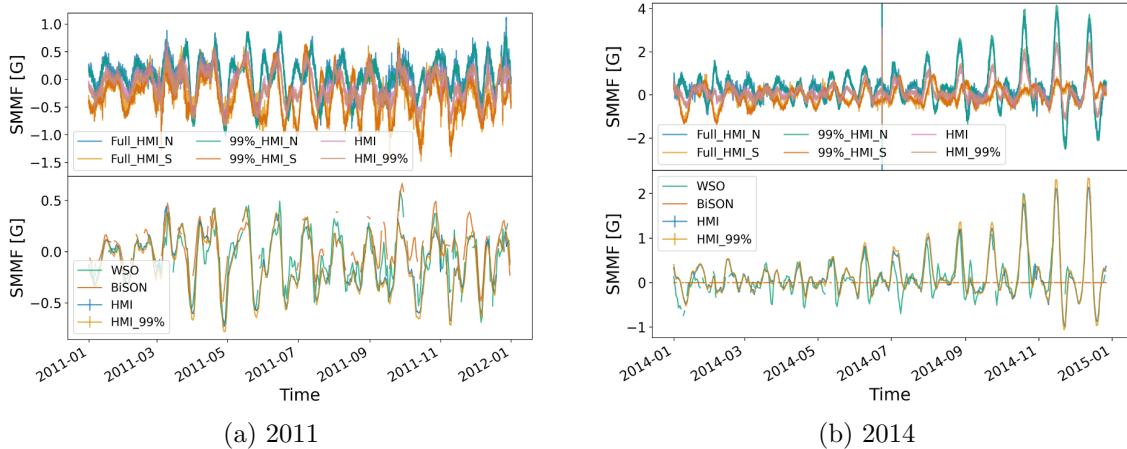


Figure 2.8: SDO/HMI SMMF split into hemispheres and compared to other SMMF sources during (a) 2011, and (b) 2014. The top panel in each figure shows the north (N), south (S), and total disk-averaged mean magnetic field, for both the full solar disk and from pixels within 99% of solar radius. The bottom panels show a comparison between the SMMF, as observed BiSON, Wilcox Solar Observatory (WSO), and HMI (full disk and the 99% disk).

The hemispheric contributions to the total, disk-averaged, SMMF can be seen in Figure 2.8 to track each other during 2011, and both become positive or negative. By contrast, when observing the hemispheric contributions to the full SMMF in 2014, we see that there are periods of strong anti correlation between the Northern

and Southern Hemispheres. This plot aids in our understanding of how the r modes would be manifested in the power spectrum due to the variation of the B_0 angle.

As there are periods of both strong correlation and strong anti correlation between the two hemispheres, this is a good indication that the r mode signal would result in a central frequency with sidebands due to the correlation between North and South. But due to periods of anti correlation between North and South, there should also be frequency splitting in the power spectrum, but this is dependent on how prevalent the anti correlation is over the entire solar cycle. It is therefore possible to conclude that we are confident we are observing the $l = 2 = m$ r mode.

As a further point, we see that there are both strong correlations and strong anti correlations between the Northern and Southern Hemispheres, however this does not necessarily mean that the r mode signal would directly manifest itself in the same way. We can see from Figure 2.5 that if the r mode observations are constrained to active latitude bands, closer to the equator, then the effects of the B_0 are less prominent.

2.6.2 Rossby Modes in Other Sources of SMMF Data

To further investigate whether the observation of the $l = 2 = m$ r mode is real, a comparison was made between the power spectrum of the BiSON observations of the SMMF and those from WSO and SDO/HMI, to determine whether the suspected r mode is visible. In the case of the WSO, the power spectrum was computed over the same observing epoch as the BiSON data (i.e. from 1992 – 2013); however SDO was not launched until 2010, so for HMI the power spectrum was computed on data from 2010 – 2020, hence at approximately half the frequency resolution of WSO and BiSON.

Figure 2.9 shows the comparison of the WSO and HMI power spectra reflected around the x-axis against the BiSON power spectrum. In both cases we see a good agreement between the different sets of data on the location of the rotational mode

in the SMMF, but there does not appear to be a visible r mode for the WSO or the HMI data.

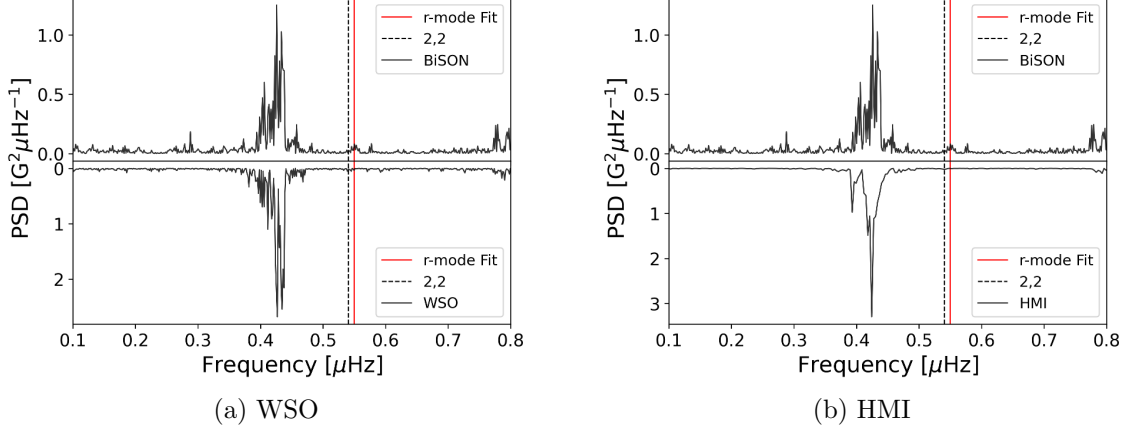


Figure 2.9: Comparison of the power spectra for BiSON, WSO, and SDO/HMI. In both figures, the top panel shows the BiSON PSD and the bottom panel shows either the WSO or HMI PSD. The dashed, black line shows the location of theoretical $l = 2 = m$ r mode frequency, and the red, solid line shows the location of the peak fit in the BiSON PSD residuals.

It was possible to use a model for the WSO SMMF [link back to SMMF chapter on the WSO SMMF analysis?] to perform the false alarm probability on the WSO PSD residuals which also confirmed the lack of existence of a peak or excess of power around the expected $l = 2 = m$ r mode frequency.

2.7 Conclusion

After removing the model for the BiSON SMMF power spectrum we investigated the residual spectrum to search for the existence of Rossby wave modes (r modes). Using a false-alarm approach we estimated the probability of finding narrow-band power. We identified the existence of a statistically significant peak which was near the $l = 2 = m$ r mode frequency calculated by Lanza et al. (2019).

Using a Lorentzian model for the peak, following the description of r mode given by Löptien et al. (2018) and Liang et al. (2019), we identified the properties of the peak, and compared them to the existing literature. The work by Lanza et al. (2019) stated that the $l = 2 = m$ r mode should be observed at a frequency of ~ 540.8

nHz, with a maximum amplitude of 24.5 cm^{-1} . The recent observations of low-degree sectoral r modes by Löptien et al. (2018) and Liang et al. (2019) claimed the line-width of the mode would be on the order of around 10 nHz, due to the e-folding lifetime of the mode being on the order of a year.

To further interrogate the inferences on the r mode in the BiSON SMMF power spectrum, we use simple simulations to determine how the r mode may manifest itself in the power spectrum, using the modulation of the signal due to the variation in the B_0 angle. Furthermore, SDO/HMI hemispheric data was employed to verify these results.

As a final check, we compared the power spectrum of the SMMF observations from BiSON to those from WSO and SDO/HMI. There was no clear signature of the $l = 2 = m$ r mode in either of the other power spectra, which rules our observation of an r mode in the BiSON SMMF very suspicious, especially as the recent observations of sectoral Rossby waves in the Sun have all used SDO/HMI data.

We leave the reader with the following points:

1. Through a series of false-alarm probability statistical tests, we have shown that there exists a statistically significant peak in the BiSON SMMF residuals spectrum which is located near the theoretical frequency of the $l = 2 = m$ r mode.
2. By modelling the peak as a Lorentzian profile we find that the peak has a central frequency of $550 \pm 16 \text{ nHz}$ (i.e. located $\sim 9.2 \text{ nHz}$ from the theoretical frequency), a line width of $5.7_{-2.9}^{+4.7} \text{ nHz}$, and an amplitude of 29 mG. This profile is within the upper limit for the amplitude of the $l = 2 = m$ r mode and the life time implied by the line width is on the order of 1–2 years, which is in agreement with the observations by Löptien et al. (2018) and Liang et al. (2019).
3. Through the analysis of simulated data and hemispheric observations of the

SMMF, we have shown that we should expect to see a prominent mode at the theoretical frequency, and not a split mode due to the effect of the B_0 variation, which supported the findings of the r mode.

4. By comparing the power spectrum of the SMMF observed by BiSON, to those of WSO and SDO/HMI, we have shown that the r mode peak is not manifested in either the WSO or SDO/HMI spectra, therefore ruling it highly unlikely that the observed peak in the BiSON spectrum is the $l = 2 = m$ r mode.

As we collect more observations of the SMMF using BiSON, the frequency resolution of the power spectrum increases. An obvious next step in this work is to collect an additional 10 years or more of SMMF observations with BiSON, to further investigate if this suspected mode remains resolved, or whether it diminishes into the noise.

A Simulations of the Artificial SMMF

A.1 Model

The artificial data used in the simulations of the SMMF was created using 2 very simplistic models, either separately or in combination, which are physically motivated by sunspots and active regions on the solar surface:

1. **Cosine**: in this model a source was simulated as a single region which appears on the visible disk from one limb, traversing across the disk, before disappearing off the other limb (see Fig. A.1a). The physical motivation for this would be a single, concentrated source of imbalanced magnetic flux. This method induces no sign change of the simulated source; it remains the same polarity always. This was simulated as a rectified sinusoidal signal, with a 50% duty cycle (i.e. it is only visible during times on near-side of the disk).
2. **Sign change**: in this model a source was simulated as 2 regions of opposite polarity, such as sunspot pairs. The leading region contributes more at the start of the transit, and the trailing source contributes more at the end of the transit; hence at the middle of the transit we assume there is a sign change in the overall signal, see Fig. A.1b. This was simulated as a rectified sinusoidal signal, and was multiplied by a cosinusoidal signal of the same period to provide the projection of the pair of regions. This operation results in a rectified sinusoidal signal with half the period.

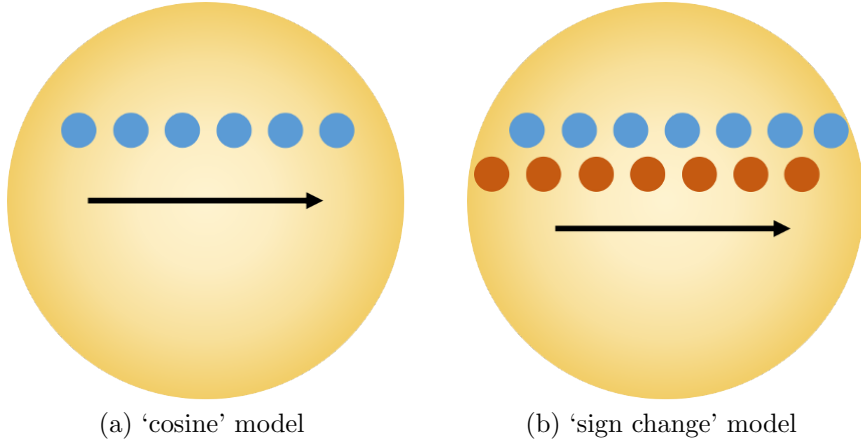


Figure A.1: Schematic representations of the two models of the artificial SMMF. (a) shows the cosine model with a single source of constant polarity transiting the visible disc. (b) shown the sign change model whereby there are 2 regions of opposite polarity transiting the disc, and their contribution to the SMMF changes during the transit.

In the simulations there were several variables which allowed us to change the physics of the simulations. These were:

- N : Number of sources
- t_0 : Start time of source
- A : Amplitude of sources
- λ : Latitude of sources
- τ : Decay time of sources
- ϕ : Additional phase of sources

Using these variables, the mathematical form of the simulation for a single source is expressed by equation (A.1) and equation (A.2). In these equations $t' = t - t_0$, $\Pi_{P/2}(t)$ is a window function to define the transit period of the simulated source on the visible side of the solar disk, III_P is a Dirac comb of frequency, P , and $\Pi_T(t)$ is a window function defining the total observation period. The time series of a single modelled source for each model is shown in Figure A.1.

$$B_{\text{cosine}}(t) = \left[A e^{-t'/\tau} \left(\cos \left(\frac{2\pi}{P} t' + \phi \right) \Pi_{P/2}(t) \right) * \text{III}_P \right] \times \Pi_T(t) \quad (\text{A.1})$$

$$B_{\text{sign-change}}(t) = \left[A e^{-t'/\tau} \left(\cos\left(\frac{2\pi}{P}t' + \phi\right) \sin\left(\frac{2\pi}{P}t' + \phi\right) \Pi_{P/2}(t) \right) * \text{III}_P \right] * \Pi_T(t) \quad (\text{A.2})$$

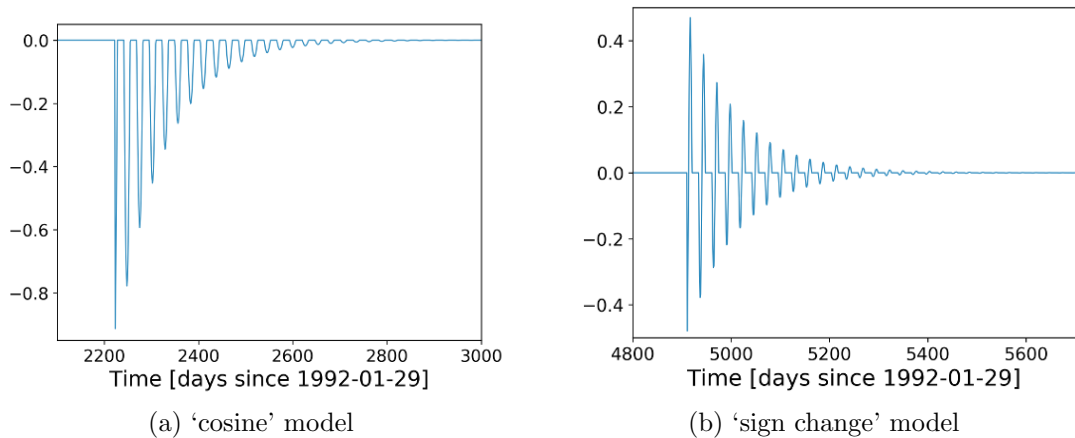


Figure A.2: A single realisation of (a) the cosine model, and (b) the sign change model.

A.2 Configuration of the Simulations

A flowchart describing the steps in the simulations is shown in Figure A.3. The simulations require the user to select the number of sources to be modelled. Using this information, the user selects whether to draw N seed/start times (t_0) from either a kernel density estimate (KDE) of the SSN, or from a uniform distribution between the start and end times.

From the generated seed times, latitudes are computed using a model for the migration of spots during the Solar Cycle (Li et al., 2001b), and the differential rotation frequency at that latitude is taken from a model of the solar differential rotation (Snodgrass, 1983).

Values are then assigned for the phase, amplitude, and decay time of each source (the user can set these parameters, or it is also possible to randomly select them from a distribution). Each individual source is then simulated according to equation (A.1) or equation (A.2), and the full time-series is computed by adding all N sources together. Finally, a burn-in period is removed, which allows the artificial SMMF to settle prior to the start of ‘observations’, and then we can inject gaps into the artificial time series that are concurrent with the gaps in the BiSON observations.

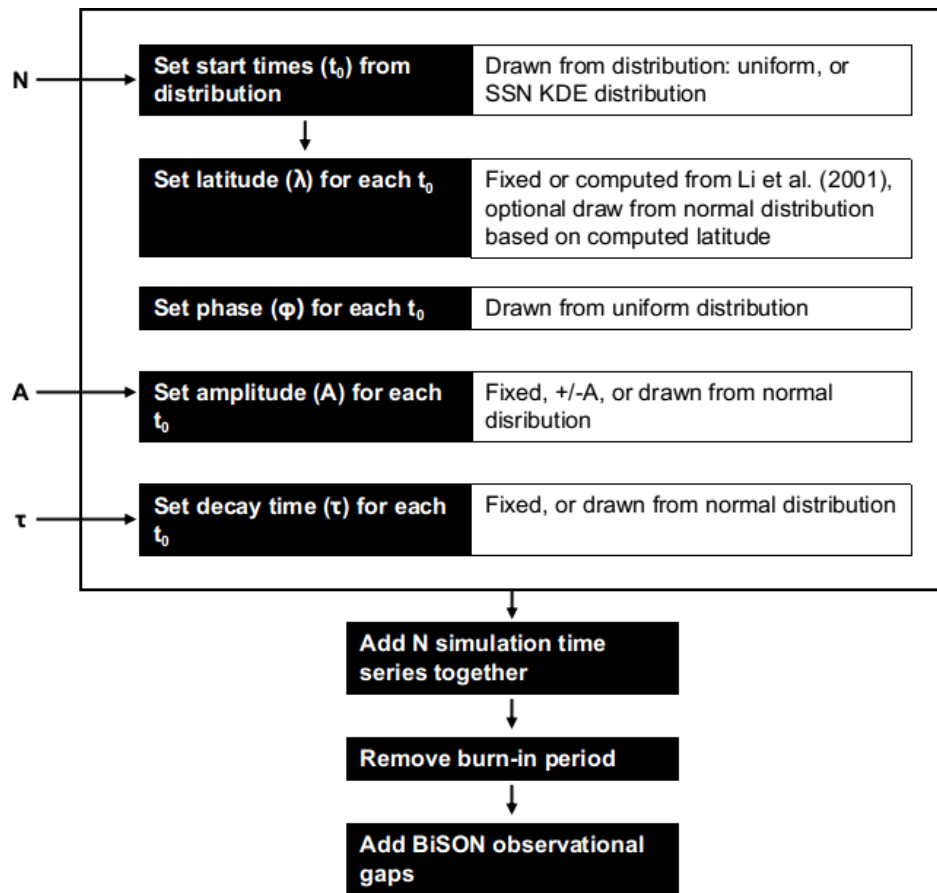
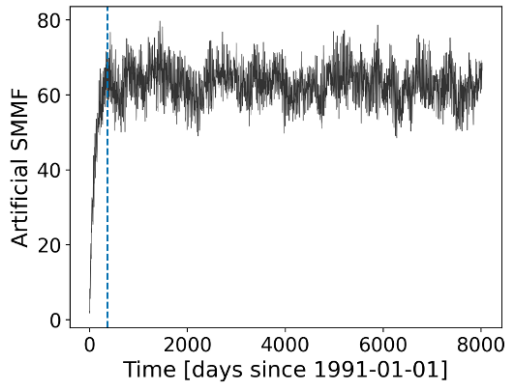


Figure A.3: ...

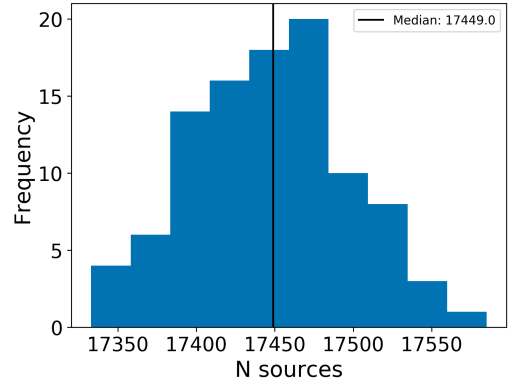
The aim of creating artificial data was to produce a representative power spectrum to that of the BiSON SMMF. We assume that the sources of the SMMF are active regions of magnetic flux, therefore we aimed to produce a time series that physically represented these sources, i.e. comparable to the sun spot number. To do this we produced an average number of sources on the visible disc during close to

the sunspot number. At solar maximum during cycle 23, the number of daily spots on the disc is around 150 – 200.

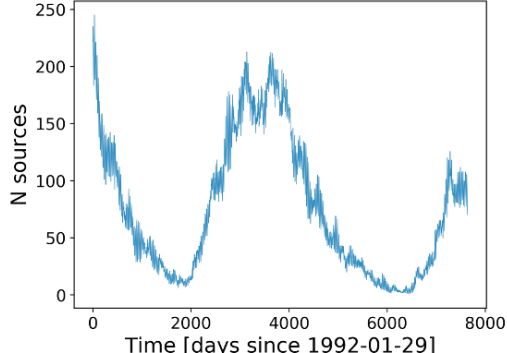
Including a year for burn-in, such that the interferences between the sources stabilises (see Figure A.4a) we chose to select $N = 20000$ and $\tau = 100$ days, which produces a median total of ~ 17450 sources over the BiSON observational epoch of 7633 days, and an average of around 150 – 200 sources per day on the visible disc during solar cycle 23 maximum, as shown in Fig. A.4.



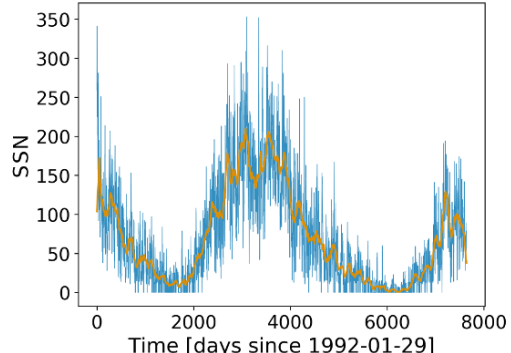
(a) Burn-in



(b) Number of sources in the simulation after burn-in



(c) Sources on the visible disc



(d) Sunspot number

Figure A.4: (a) the burn-in period required to ensure that the interference of sources stabilises. (b) histogram of the number of sources which remain in the simulation (out of the 20000 input), after the burn-in is removed. (c)

A.3 Outputs

The two different models give different features in the power spectrum which can be seen in Fig. A.5. These limit spectra have been made by combining 100 realisations of the power spectrum. Each individual power spectrum was made using only a single source starting at $t_0 = 0$, and allowing only the phase to vary between the different realisations.

It is clear that the cosine model produces a strong peak at the rotational period in the simulation, and a harmonic peak at twice that frequency. This model also produces a significant amount of power at low frequency due to the non-zero mean of the simulated time series.

On the other hand, the sign change model has near-zero low frequency power due to the \sim zero mean of the time series. The sign change model also produces a strong peak at half the period of rotation in the simulation. There is a smaller peak at the rotational period and harmonics of the rotation at 3 times the rotational period.

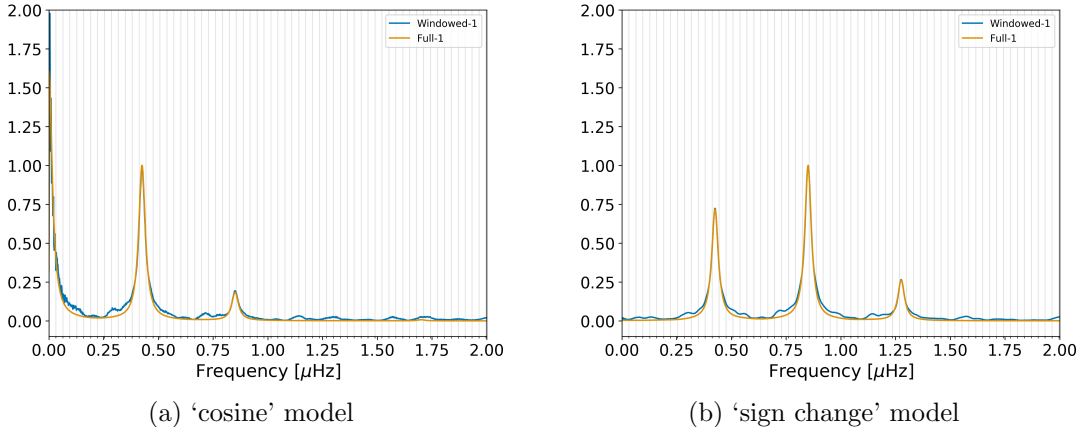


Figure A.5: Limit spectrum from 100 realisations of the cosine model (a) and the sign change model (b) using a single source in each model.

Bibliography

- Appourchaux T., 2003, *Astronomy and Astrophysics*, 412, 903
- Barnes a. W. T., et al., 2020, *ApJ*, 890, 68
- Basu S., Chaplin W. J., 2017, *Asteroseismic Data Analysis: Foundations and Techniques*
- Beck J. G., 2000, *Solar Physics*, 191, 47
- Bose S., Nagaraju K., 2018, *The Astrophysical Journal*, 862, 35
- Brookes J. R., Isaak G. R., Raay H. B. v. d., 1976, *Nature*, 259, 92
- Brookes J. R., Isaak G. R., van der Raay H. B., 1978, *Mon Not R Astron Soc*, 185, 1
- Brown T. M., Christensen-Dalsgaard J., Dziembowski W. A., Goode P., Gough D. O., Morrow C. A., 1989, *The Astrophysical Journal*, 343, 526
- Chaplin W. J., Appourchaux T., 1999, *Mon Not R Astron Soc*, 309, 761
- Chaplin W. J., et al., 1996, *Solar Physics*, 168, 1
- Chaplin W. J., Dumbill A. M., Elsworth Y., Isaak G. R., McLeod C. P., Miller B. A., New R., Pintr B., 2003, *Mon Not R Astron Soc*, 343, 813
- Chaplin W. J., Elsworth Y., Isaak G. R., Miller B. A., New R., Pintr B., 2005, *Mon Not R Astron Soc*, 359, 607
- Chaplin W. J., Elsworth Y., New R., Toutain T., 2008, *Monthly Notices of the Royal Astronomical Society*, 384, 1668
- Davies G. R., Broomhall A. M., Chaplin W. J., Elsworth Y., Hale S. J., 2014a, *Monthly Notices of the Royal Astronomical Society*, 439, 2025
- Davies G. R., Chaplin W. J., Elsworth Y., Hale S. J., 2014b, *Mon Not R Astron Soc*, 441, 3009
- Dumbill A. M., 1999, PhD thesis, School of Physics and Space Research, University of Birmingham
- Duvall Jr. T. L., Jefferies S. M., Harvey J. W., Osaki Y., Pomerantz M. A., 1993, *The Astrophysical Journal*, 410, 829
- Elsworth Y., Howe R., Isaak G. R., McLeod C. P., Miller B. A., van der Raay H. B., Wheeler S. J., New R., 1995a. p. 392, <http://adsabs.harvard.edu/abs/1995ASPC...76..392E>

- Elsworth Y., Howe R., Isaak G. R., McLeod C. P., Miller B. A., New R., Wheeler S. J., 1995b, *Astronomy and Astrophysics Supplement Series*, 113, 379
- Foreman-Mackey D., Hogg D. W., Lang D., Goodman J., 2013, *Publications of the Astronomical Society of the Pacific*, 125, 306
- Garca R. A., et al., 1999, *Astronomy and Astrophysics*, 346, 626
- Hale S. J., Howe R., Chaplin W. J., Davies G. R., Elsworth Y., 2016, *Solar Physics*, 291, 1
- Hanasoge S., Mandal K., 2019, *The Astrophysical Journal Letters*, 871, L32
- Handberg R., Campante T. L., 2011, *Astronomy & Astrophysics*, 527, A56
- Harvey K. L., Zwaan C., 1993, *Solar Physics*, 148, 85
- Hathaway D. H., Choudhary D. P., 2008, *Sol Phys*, 250, 269
- Hathaway D. H., Upton L. A., 2020, arXiv e-prints, 2006, arXiv:2006.06084
- Howard R. F., 2001, in , *The Encyclopedia of Astronomy and Astrophysics*. IOP Publishing Ltd, doi:10.1888/0333750888/2297, <http://eaa.crcpress.com/0333750888/2297>
- Howe R., 2009, *Living Reviews in Solar Physics*, 6
- Howe R., Davies G. R., Chaplin W. J., Elsworth Y. P., Hale S. J., 2015, *Mon Not R Astron Soc*, 454, 4120
- Howe R., et al., 2020, *Mon Not R Astron Soc Lett*, 493, L49
- Kotov V. A., 2008, *Astron. Rep.*, 52, 419
- Kotov V. A., 2012, *Bull.Crim. Astrophys. Observ.*, 108, 20
- Kutsenko A. S., Abramenko V. I., Yurchyshyn V. B., 2017, *Sol Phys*, 292, 121
- Lanza A. F., Gizon L., Zaqrashvili T. V., Liang Z.-C., Rodenbeck K., 2019, *A&A*, 623, A50
- Li K. J., Yun H. S., Gu X. M., 2001a, *AJ*, 122, 2115
- Li K. J., Yun H. S., Gu X. M., 2001b, *AJ*, 122, 2115
- Liang Z.-C., Gizon L., Birch A. C., Duvall T. L., 2019, *A&A*, 626, A3
- Löptien B., Gizon L., Birch A. C., Schou J., Proxauf B., Duvall T. L., Bogart R. S., Christensen U. R., 2018, *Nature Astronomy*, 2, 568
- Lund M. N., Chaplin W. J., Hale S. J., Davies G. R., Elsworth Y. P., Howe R., 2017, *Mon Not R Astron Soc*, 472, 3256
- Maunder E. W., 1904, *Mon Not R Astron Soc*, 64, 747
- McIntosh S. W., et al., 2014, *ApJ*, 792, 12

- Plachinda S., Pankov N., Baklanova D., 2011, Astronomische Nachrichten, 332, 918
- Rossby C.-G., Collaborators 1939, J Mar Res, 2, 38
- Salvatier J., Wiecki T. V., Fonnesbeck C., 2016, PeerJ Comput. Sci., 2, e55
- Scherrer P. H., Wilcox J. M., Howard R., 1972, Sol Phys, 22, 418
- Scherrer P. H., Wilcox J. M., Kotov V., Severnyj A. B., Severny A. B., Howard R., 1977a, Solar Physics, 52, 3
- Scherrer P. H., Wilcox J. M., Svalgaard L., Duvall Jr. T. L., Dittmer P. H., Gustafson E. K., 1977b, Solar Physics, 54, 353
- Severny A. B., 1971, Quarterly Journal of the Royal Astronomical Society, 12, 363
- Snodgrass H. B., 1983, The Astrophysical Journal, 270, 288
- Strohmayer T., Mahmoodifar S., 2014, A Neutron Star Oscillation Mode During a Superburst, <https://slideplayer.com/slide/10313230/>
- Svalgaard L., Wilcox J. M., Scherrer P. H., Howard R., 1975, Sol Phys, 45, 83
- Thomas A. E. L., et al., 2019, Mon Not R Astron Soc, 485, 3857
- Wu C. J., Usoskin I. G., Krivova N., Kovaltsov G. A., Baroni M., Bard E., Solanki S. K., 2018, A&A, 615, A93
- Xiang N. B., Qu Z. N., 2016, AJ, 151, 76
- Xie J. L., Shi X. J., Xu J. C., 2017, The Astronomical Journal, 153, 171
- Zwaan C., 1981, NASA Special Publication, 450